A decorative graphic on the right side of the page. It features three concentric circles in shades of blue. Two thin blue lines originate from the top left and extend towards the circles. A larger blue circle is at the top right, a medium one in the middle, and a large one at the bottom right. The bottom right circle is partially cut off by the page edge.

Modelling Flow and Sediment Transport in the St. Marys River near Sault Ste Marie, Ontario, Canada

A flow and sediment transport modelling approach is proposed for the St. Marys River to determine the physical stability of the surface sediment in the river. This study will determine whether the top 0-10 cm of sediment will erode away under various flows, ice scour and changes in water levels exposing deeper more contaminated sediment to aquatic organisms. The results of the study will assist in the development of management strategies for contaminated sediment deposits in St. Marys River.

Based on measured flow and sediment bed characteristics, a two dimensional flow modelling system called TABS-MD with SMS user interface is selected for the modelling approach. TABS-MD consists of a two dimensional hydrodynamic flow model (RMA2) and a fine sediment transport model (RMA4). Details of these models and their application to the St. Marys River are described in this report. The predicted bed shear stresses for different flow-rates with their associated water levels are compared with the critical shear stress for erosion of sediment to assess its stability under different flow regimes. Effects of ice cover on flow and sediment stability are also assessed. Potential impacts of ice scour process are discussed. The results of this study indicated that lower layers of contaminated fine sediment deposits near the banks of the river are stable under different flows tested in this study.

Bommanna Krishnappan
2/24/2011

TABLE OF CONTENTS

1.0 INTRODUCTION	1
2.0 FLOW DATA OF USACE	4
2.1. SELECTION OF A FLOW AND SEDIMENT TRANSPORT MODEL FOR THE ST. MARYS RIVER.....	11
3.0 DETAILS OF TABS-MD WITH SMS USER INTERFACE	11
3.1 RMA2 MODEL	11
3.2 RMA4 MODEL	13
3.3 SMS USER INTERFACE.....	14
4.0 MODELLING DOMAIN AND GEOMETRY DATA.....	14
5.0 SPECIFICATION OF BOUNDARY CONDITIONS	17
6.0 CALIBRATION OF THE MODEL	20
7.0 RESULTS FROM THE MODEL SIMULATIONS.....	21
8.0 ASSESSMENT OF STABILITY OF SEDIMENT DEPOSITS	31
8.1 VIDEO IMAGING OF THE RIVER BED	31
8.2 GRAB SAMPLING OF THE RIVER BED SEDIMENT	36
8.3 COMPUTATION OF CRITICAL SHEAR STRESS FOR EROSION FOR NON-COHESIVE SEDIMENT	42
8.4 MEASUREMENT OF CRITICAL SHEAR STRESS FOR EROSION OF COHESIVE SEDIMENT	45
8.4.1 Instrumentation	45
8.4.2 Calibration.....	46
8.4.3 Operation of the flume in the field.....	47
9.0 IMPACTS OF WATER LEVEL CHANGES	51
10.0 IMPACTS OF ICE COVER ON SEDIMENT STABILITY	51
10.1. IMPACTS OF ICE SCOUR	58
11.0 TRANSPORT CHARACTERISTICS OF ERODED AND/OR INTRODUCED SEDIMENT IN THE RIVER	59
12.0 SUMMARY AND CONCLUSIONS	65
ACKNOWLEDGEMENTS	65
REFERENCES.....	66
APPENDIX-A.....	67
APPENDIX-B	82
APPENDIX-C	97

LIST OF FIGURES

FIG. 1. MAP SHOWING THE ST. MARYS RIVER.	2
FIG. 2. AERIAL VIEW OF VARIOUS STRUCTURES BUILT ACROSS THE ST. MARYS RIVER NEAR SAULT STE MARIE.	3
FIG. 3. GOOGLE EARTH IMAGE SHOWING THE ADCP TRANSECTS (ADCP 310, ADCP 340, ADCP 330, ADCP 360 AND ADCP 350AS INDICATED BY THE YELLOW “PLACE-MARKS”).	5
FIG. 4. CONTOUR PLOT OF MAGNITUDE OF VELOCITY VECTORS IN THE CROSS SECTIONAL PLANE ACROSS TRANSECT 310 (LOOKING DOWNSTREAM).	5
FIG. 5. “STICK SHIP TRACK” DIAGRAM FOR TRANSECT 310.	6
FIG. 6. CONTOUR PLOT OF MAGNITUDE OF VELOCITY VECTORS IN THE CROSS SECTIONAL PLANE ACROSS TRANSECT 340 (LOOKING DOWNSTREAM).	6
FIG. 7. “STICK SHIP TRACK” DIAGRAM FOR TRANSECT 340.	7
FIG. 8. CONTOUR PLOT OF MAGNITUDE OF VELOCITY VECTORS IN THE CROSS SECTIONAL PLANE ACROSS TRANSECT 330 IN THE NAVIGATIONAL CHANNEL (LOOKING DOWNSTREAM).	7
FIG. 9. “STICK SHIP TRACK” DIAGRAM FOR TRANSECT 330.	8
FIG. 10. CONTOUR PLOT OF MAGNITUDE OF VELOCITY VECTORS IN THE CROSS SECTIONAL PLANE ACROSS TRANSECT 360 IN THE CHANNEL NORTH OF SUGAR ISLAND (LOOKING DOWNSTREAM).	8
FIG. 11. “STICK SHIP TRACK” DIAGRAM FOR TRANSECT 360.	9
FIG. 12. CONTOUR PLOT OF MAGNITUDE OF VELOCITY VECTORS IN THE CROSS SECTIONAL PLANE ACROSS TRANSECT 350 IN THE CHANNEL DOWNSTREAM OF LITTLE LAKE GEORGE (LOOKING DOWNSTREAM).	9
FIG. 13. “STICK SHIP TRACK” DIAGRAM FOR TRANSECT 350.	10
FIG. 14. RIVER REACH SELECTED AS MODELLING DOMAIN WITH BATHYMETRY DATA (SHOWN AS GREEN POINTS).	15
FIG. 15A UPPER PART OF THE FINITE ELEMENT MESH GENERATED USING SMS.	16
FIG. 15B. MIDDLE PART OF THE FINITE ELEMENT GRID GENERATED USING SMS.	16
FIG. 15C. THE LOWER PART OF THE FINITE ELEMENT MESH GENERATED USING SMS.	17
FIG. 17. MONTHLY AVERAGE FLOW RATE THROUGH EDISON SAULT ELECTRIC COMPANY POWER PLANT.	19
FIG. 18. COVERAGE OF THE COARSE GRID RMA2 MODEL DEVELOPED BY USACE FOR THE ENTIRE ST. MARYS RIVER SYSTEM (ERIC TAURIANEN).	20
FIG. 19. A TYPICAL AGREEMENT BETWEEN THE MODEL PREDICTION AND THE ADCP DATA MEASURED IN ONE OF THE TRANSECTS IN THE ST. MARYS RIVER.	21
FIG. 20 A. VELOCITY VECTORS PREDICTED BY THE MODEL FOR THE UPPER PART OF THE FLOW DOMAIN.	22
FIG. 20B. VELOCITY VECTORS PREDICTED BY THE MODEL FOR THE MIDDLE PART OF THE FLOW DOMAIN.	23
FIG. 20C. VELOCITY VECTORS PREDICTED BY THE MODEL FOR THE LOWER PART OF THE FLOW DOMAIN.	23
FIG. 21. COMPUTED MAGNITUDE OF FLOW VELOCITIES IN THE COMPUTATIONAL DOMAIN FOR AVERAGE FLOW CONDITIONS.	24
FIG. 22. COMPUTED FLOW DEPTHS OVER THE COMPUTATIONAL FLOW DOMAIN FOR AVERAGE FLOW CONDITION.	25
FIG. 23. COMPUTED WATER SURFACE ELEVATIONS OVER THE COMPUTATIONAL DOMAIN FOR THE AVERAGE FLOW CONDITION.	26
FIG. 24. COMPUTED BED SHEAR STRESS DISTRIBUTION OVER THE COMPUTATIONAL DOMAIN FOR AVERAGE FLOW CONDITION.	27
FIG. 25. VARIATION OF SIMULATED VELOCITY MAGNITUDES ACROSS THE UPPER PART OF THE LOWER ST. MARYS RIVER. .	28

FIG. 26. BED SHEAR STRESS VARIATION ACROSS A SECTION IN THE UPPER PART OF THE LOWER ST. MARYS RIVER.	29
FIG. 27. COMPARISON OF VELOCITY MAGNITUDE DIFFERENT FLOW CONDITIONS AS PREDICTED BY THE MODEL.	30
FIG. 28. COMPARISON OF BED SHEAR STRESSES FOR DIFFERENT FLOW CONDITIONS AS PREDICTED BY THE MODEL.....	31
FIG. 29. VIDEO IMAGING SYSTEM DEVELOPED BY ENVIRONMENT CANADA (HANS BIBERHOFER)	32
FIG. 30. LOCATIONS OF TRANSECTS WHERE THE VIDEO IMAGING WAS CARRIED OUT (YELLOW LINES).....	33
FIG. 31. AN IMAGE GRABBED FROM A VIDEO CLIP OF TRANSECT 2.	34
FIG. 32. AN IMAGE GRABBED FROM A VIDEO CLIP OF TRANSECT 7.....	34
FIG. 33. GRABBED IMAGE FROM VIDEO CLIP OF TRANSECT 7 SHOWING THE VEGETATION AND THE FINE SEDIMENT CLOUD CREATED WHEN THE FISH WEIGHT HIT THE RIVER BED.	35
FIG. 34. GRABBED IMAGE FROM THE VIDEO CLIP OF TRANSECT 9 SHOWING THE PRESENCE OF ANGULAR ROCKS.	35
FIG. 35. A PHOTOGRAPH OF GRAB SAMPLE COLLECTED AT TRANSECT NO. 2 (SAMPLE ID: SMR-T2-2)	37
FIG. 36. A PHOTOGRAPH OF GRAB SAMPLE COLLECTED AT TRANSECT 3 (SAMPLE ID: SMR-T3-1)	38
FIG. 37. A PHOTOGRAPH OF GRAB SAMPLE COLLECTED AT TRANSECT 14 (SAMPLE ID: SMR-T14-3).	38
FIG. 38. AN EXAMPLE OF THE RESULTS FROM THE SIZE ANALYSIS OF THE GRAB SAMPLES.	40
FIG. 39. COMPARISON OF BED SHEAR STRESSES WITH CRITICAL SHEAR STRESSES FOR EROSION OF NON-COHESIVE GRAB SAMPLES.	44
FIG. 40. A PHOTOGRAPH OF THE IN-SITU EROSION FLUME.	45
FIG.41. RELATIONSHIP BETWEEN THE FLOW RATE AND THE BED SHEAR STRESS	46
FIG. 42. RELATIONSHIP BETWEEN THE FLOW RATE AND THE READ-OUT IN “FLOW DEGREES”.	47
FIG.43. DEPLOYMENT OF THE IN-SITU EROSION FLUME.	48
FIG. 44. LOCATIONS OF THE IN-SITU EROSION FLUME MEASUREMENT SITES (SHOWN AS WHITE DOTS).....	49
FIG. 45. SHEAR STRESS DISTRIBUTION OF ICE-COVERED FLOW UNDER AVERAGE FLOW CONDITION.	53
FIG. 46. SHEAR STRESS DISTRIBUTION OF ICE COVERED FLOW UNDER LOW FLOW CONDITION.	54
FIG. 47. SHEAR STRESS DISTRIBUTION OF ICE COVERED FLOW UNDER HIGH FLOW CONDITION.	55
FIG. 48. SHEAR STRESS DISTRIBUTION FOR ICE COVERED FLOWS ALONG THE TRANSECT A.	56
FIG. 49. COMPARISON OF BED SHEAR STRESS WITH CRITICAL SHEAR STRESS FOR ICE-COVERED FLOWS.	57
FIG. 50. SIMULATION OF SEDIMENT TRANSPORT IN ST. MARYS RIVER: ELAPSED TIME = 0.125 HRS.	60
FIG. 51. SIMULATION OF SEDIMENT TRANSPORT IN ST. MARYS RIVER: ELAPSED TIME = 2.0 HRS.	61
FIG. 52. SIMULATION OF SEDIMENT TRANSPORT IN ST. MARYS RIVER: ELAPSED TIME = 4.0 HRS.	62
FIG. 54. SIMULATION OF SEDIMENT TRANSPORT IN ST. MARYS RIVER: ELAPSED TIME = 12.0 HRS.	64
FIG. A1A. VELOCITY VECTORS PREDICTED BY THE MODEL FOR THE UPPER PART OF THE COMPUTATIONAL DOMAIN FOR LOW FLOW CONDITION.	68
FIG. A1B. VELOCITY VECTORS PREDICTED BY THE MODEL FOR THE MIDDLE PART OF THE COMPUTATIONAL DOMAIN FOR LOW FLOW CONDITION.	69
FIG. A1C. VELOCITY VECTORS PREDICTED BY THE MODEL FOR THE LOWER PART OF THE COMPUTATIONAL DOMAIN FOR LOW FLOW CONDITION.	70
FIG. A2. DISTRIBUTION OF VELOCITY MAGNITUDE PREDICTED BY THE MODEL FOR THE LOW FLOW CONDITION.	71
FIG. A3. DISTRIBUTION OF WATER DEPTH PREDICTED BY THE MODEL FOR THE LOW FLOW CONDITION.	72
FIG.A4 DISTRIBUTION OF WATER SURFACE ELEVATION PREDICTED BY THE MODEL FOR LOW FLOW CONDITION.....	73
FIG.A5. DISTRIBUTION OF BED SHEAR STRESS PREDICTED BY THE MODEL FOR LOW FLOW CONDITION.	74

FIG. A6A. PREDICTED VELOCITY VECTORS IN THE UPPER PART OF THE COMPUTATIONAL DOMAIN FOR THE HIGH FLOW CONDITION.....	75
FIG. A6B. PREDICTED VELOCITY VECTORS IN THE MIDDLE PART OF THE COMPUTATIONAL DOMAIN FOR THE HIGH FLOW CONDITION.....	76
FIG. A6C. PREDICTED VELOCITY VECTORS IN THE LOWER PART OF THE COMPUTATIONAL DOMAIN FOR THE HIGH FLOW CONDITION.....	77
FIG. A7. PREDICTED VELOCITY MAGNITUDES BY THE MODEL FOR THE HIGH FLOW CONDITION.	78
FIG. A8. PREDICTED FLOW DEPTH DISTRIBUTION FOR THE HIGH FLOW CONDITION.	79
FIG. A9. PREDICTED WATER SURFACE ELEVATION BY THE MODEL FOR THE HIGH FLOW CONDITION.	80
FIG. A10. PREDICTED BED SHEAR STRESS DISTRIBUTIONS FOR THE HIGH FLOW CONDITION.	81
FIG. B1. PHOTOGRAPH OF GRAB SAMPLE COLLECTED AT TRANSECT 2 (SAMPLE ID: SMR-T2-2).....	83
FIG. B2. PHOTOGRAPH OF THE GRAB SAMPLE COLLECTED AT TRANSECT 2 (SAMPLE ID: SMR-T2-3).	83
FIG. B3. PHOTOGRAPH OF THE GRAB SAMPLE COLLECTED AT TRANSECT 3 (SAMPLE ID: SMR-T3-1).....	84
FIG. B4. PHOTOGRAPH OF THE GRAB SAMPLE COLLECTED AT TRANSECT 3 (SAMPLE ID: SMR-T3-2).	84
FIG. B5. PHOTOGRAPH OF THE GRAB SAMPLE COLLECTED AT TRANSECT 3 (SAMPLE ID: SMR-T3-3).	85
FIG. B6. PHOTOGRAPH OF THE GRAB SAMPLE COLLECTED AT TRANSECT 4 (SAMPLE ID: SMR-T4-1).	85
FIG. B7. PHOTOGRAPH OF THE GRAB SAMPLE COLLECTED AT TRANSECT 4 (SAMPLE ID: SMR-T4-2).	86
FIG. B8. PHOTOGRAPH OF THE GRAB SAMPLE COLLECTED AT TRANSECT 4 (SAMPLE ID: SMR-T4-3).	86
FIG. B9. PHOTOGRAPH OF THE GRAB SAMPLE COLLECTED AT TRANSECT 5 (SAMPLE ID: SMR-T5-1).	87
FIG. B10. PHOTOGRAPH OF THE GRAB SAMPLE COLLECTED AT TRANSECT 9 (SAMPLE ID: SMR-T9-1).....	87
FIG. B11. PHOTOGRAPH OF THE GRAB SAMPLE COLLECTED AT TRANSECT 9 (SAMPLE ID: SMR-T9-2).	88
FIG. B12. PHOTOGRAPH OF THE GRAB SAMPLE COLLECTED AT TRANSECT 10 (SAMPLE ID: SMR-T10-1).	88
FIG. B13. PHOTOGRAPH OF THE GRAB SAMPLE COLLECTED AT TRANSECT 10 (SAMPLE ID: SMR-T10-2).	89
FIG. B14. PHOTOGRAPH OF THE GRAB SAMPLE COLLECTED AT TRANSECT 10 (SAMPLE ID: SMR-T10-3).	89
FIG. B15. PHOTOGRAPH OF THE GRAB SAMPLE COLLECTED AT TRANSECT 10 (SAMPLE ID: SMR-T10-4).	90
FIG. B16. PHOTOGRAPH OF THE GRAB SAMPLE COLLECTED AT TRANSECT 11 (SAMPLE ID: SMR-T11-1).	90
FIG. B17. PHOTOGRAPH OF THE GRAB SAMPLE COLLECTED AT TRANSECT 11 (SAMPLE ID: SMR-T11-2).	91
FIG. B18. PHOTOGRAPH OF THE GRAB SAMPLE COLLECTED AT TRANSECT 11 (SAMPLE ID: SMR-T11-3).	91
FIG. B19. PHOTOGRAPH OF THE GRAB SAMPLE COLLECTED AT TRANSECT 12 (SAMPLE ID: SMR-T12-1).	92
FIG. B20. PHOTOGRAPH OF THE GRAB SAMPLE COLLECTED AT TRANSECT 12 (SAMPLE ID: SMR-T12-2).	92
FIG. B21. PHOTOGRAPH OF THE GRAB SAMPLE COLLECTED AT TRANSECT 12 (SAMPLE ID: SMR-T12-3).	93
FIG. B22. PHOTOGRAPH OF THE GRAB SAMPLE COLLECTED AT TRANSECT 13 (SAMPLE ID: SMR-T13-1).	93
FIG. B23. PHOTOGRAPH OF THE GRAB SAMPLE COLLECTED AT TRANSECT 13 (SAMPLE ID: SMR-T13-2).	94
FIG. B24. PHOTOGRAPH OF THE GRAB SAMPLE COLLECTED AT TRANSECT 13 (SAMPLE ID: SMR-T13-3).	94
FIG. B25. PHOTOGRAPH OF THE GRAB SAMPLE COLLECTED AT TRANSECT 14 (SAMPLE ID: SMR-T14-1).	95
FIG. B26. PHOTOGRAPH OF THE GRAB SAMPLE COLLECTED AT TRANSECT 14 (SAMPLE ID: SMR-T14-2).	95
FIG. B27. PHOTOGRAPH OF THE GRAB SAMPLE COLLECTED AT TRANSECT 14 (SAMPLE ID: SMR-T14-3).	96
FIG. C1. SIMULATION OF SEDIMENT TRANSPORT IN ST. MARYS RIVER UNDER LOW FLOW CONDITION: ELAPSED TIME = 0.125 HRS.	98
FIG. C2. SIMULATION OF SEDIMENT TRANSPORT IN ST. MARYS RIVER UNDER LOW FLOW CONDITION: ELAPSED TIME = 2.0 HRS.	99

FIG. C3. SIMULATION OF SEDIMENT TRANSPORT IN ST. MARYS RIVER UNDER LOW FLOW CONDITION: ELAPSED TIME = 4.0 HRS.	100
FIG. C4. SIMULATION OF SEDIMENT TRANSPORT IN ST. MARYS RIVER UNDER LOW FLOW CONDITION: ELAPSED TIME = 8.0 HRS.	101
FIG. C5. SIMULATION OF SEDIMENT TRANSPORT IN ST. MARYS RIVER UNDER LOW FLOW CONDITION: ELAPSED TIME = 12.0 HRS.	102
FIG. C6. SIMULATION OF SEDIMENT TRANSPORT IN ST. MARYS RIVER UNDER HIGH FLOW CONDITION: ELAPSED TIME = 0.125 HRS.	103
FIG. C7. SIMULATION OF SEDIMENT TRANSPORT IN ST. MARYS RIVER UNDER HIGH FLOW CONDITION: ELAPSED TIME = 2.0 HRS.	104
FIG. C8. SIMULATION OF SEDIMENT TRANSPORT IN ST. MARYS RIVER UNDER HIGH FLOW CONDITION: ELAPSED TIME = 4.0 HRS.	105
FIG. C9. SIMULATION OF SEDIMENT TRANSPORT IN ST. MARYS RIVER UNDER HIGH FLOW CONDITION: ELAPSED TIME = 8.0 HRS.	106
FIG. C10. SIMULATION OF SEDIMENT TRANSPORT IN ST. MARYS RIVER UNDER HIGH FLOW CONDITION: ELAPSED TIME = 12.0 HRS.	107

LIST OF TABLES

TABLE 1. SAMPLE IDENTIFICATION AND LOCATION OF GRAB SAMPLES.	36
TABLE 2. SUMMARY OF THE SIZE DISTRIBUTION DATA FOR ALL GRAB SAMPLES.	41
TABLE 3: COMPUTATION OF CRITICAL SHEAR STRESS FOR EROSION OF GRAB SAMPLES THAT ARE NON-COHESIVE.	43
TABLE 4. LOCATIONS OF FLUME SITES AND THE SHEAR STRESSES PREDICTED BY THE MODEL FOR THESE SITES.....	49
TABLE 5. LOCATION OF FLUME SITES WITH ICE-COVERED SHEAR STRESSES AND THE CRITICAL SHEAR STRESS.	58

LIST OF APPENDICES

APPENDIX-A.....	67
APPENDIX-B.....	82
APPENDIX-C.....	97

1.0 Introduction

The St. Marys River is one of the connecting channels of the Great Lakes system and it flows from Lake Superior to Lakes Huron and Michigan. It originates at the southeast corner of Lake Superior and flows in a south-easterly direction to Lake Huron (Fig.1). The river consists of two distinct reaches, an upper reach and a lower reach. The upper reach begins at the lower end of Whitefish Bay, and extends 22.5 km to the St. Marys Rapids. The river in this reach is broad and deep and it falls about 7.5 m over its distance. A rock ledge at the head of the St. Marys Rapids forms the natural control of the St. Marys River. Over the Rapids which extend a distance of 2.5 km, the river falls about 6.1 m. Around the area of the Rapids, the river has seen an extensive array of man-made structures such as bridges, navigation locks, hydro power plants and gated compensation works. An aerial view of the various structures built across the river is shown in Fig.2. The lower river flows from the foot of the St. Marys Rapids to Point Detour on Lake Huron. About four kilo-meters downstream from the foot of the St. Marys Rapids, the river divides into two channels, one flowing to the north end and the other to the west end of the Sugar Island. The flow in the northerly channel continues into Lake George and around the St. Joseph Island into North Channel, Lake Huron. The flow west of Sugar Island passes around Neebish Island into Lake Munuscong. It then flows past the St. Joseph Island and then into Lake Huron. This branch of the river serves as the navigational channel for the large commercial ships. The fall of the lower river amounts to about 50 cm over a distance of about 90 km.

The St. Marys Rapids was the site of an extensive seasonal whitefish fishery for centuries before European contact (St. Marys Fisheries Task Group Report, 2002). Thousands of Native peoples from the Great Lakes Basin and around would arrive in late spring to harvest whitefish over the summer. European settlement brought significant changes to the St. Marys River. By the mid-1800s, non-Native commercial fisheries were established by the fur trading companies. By the mid-1850s the first of several locks was completed to allow vessels past the rapids. Extensive dredging and re-aligning of channels also occurred to aid vessel navigation. Shoreline developments such as shipyards, steel production, a paper mill, a major tannery, and docking facilities degraded productive fish habitat and added additional industrial pollution to the river. Hydroelectric stations and the control of water flows also affected fish spawning and nursery habitat as well as aquatic food production (St. Marys Fisheries Task Group Report, 2002). As a result, in 1985, the International Joint Commission declared the St. Marys River an Area of Concern (AOC). In addition, the Great Lakes Water Quality Agreement between Canada and the United States stipulated that each AOC must have a Remedial Action Plan (RAP) to restore the beneficial uses of the river including addressing the management of contaminated sediments.



Fig. 1. Map showing the St. Marys River.



Fig. 2. Aerial view of various structures built across the St. Marys River near Sault Ste Marie.

Management of contaminated sediment in the St. Marys River requires better understanding of the flow field and the sediment transport characteristics of the river. Specifically, the development of management strategies for contaminated sediment relies on our understanding of the stability of the contaminated sediment deposits for different flows and ice-cover conditions. Stability of sediment deposits can be assessed by comparing the critical shear stress for erosion of the sediment deposits with the bed shear stresses induced by the flow field. The critical shear stresses for erosion of the contaminated sediment deposits in the St. Marys River were measured by Environment Canada in Burlington, Ontario (Hans Biberhofer, 2010). Bed shear stresses induced by the flow fields are best obtained by the application of mathematical models to the river. Mathematical models of river flows also yield velocity fields which are the bases for the advection and the dispersive transport of sediment in the river. Therefore, the mathematical modelling of river flows is also useful for predicting the transport of eroded and/or introduced sediment to the river flow and their eventual deposition to the river bed in low flow areas.

Selection of a mathematical model for predicting flow and sediment transport in the St. Marys River was based on available flow data for the river. Flow data for the river was obtained from the United States Army Corps of Engineers (USACE) in the Detroit District (Eric Tauriainen). The data was collected in July, 2009 as part of a flow investigation to install a permanent side looking Acoustic Doppler Current Profiler (ADCP) in the lower reach of the river for the International Joint Commission's Upper Great Lakes Water Level Regulation Study. A detailed examination of the flow data is undertaken in this study to gain an understanding of the flow field, which in turn will serve as a guide for the selection of an appropriate flow model for the St. Marys River.

2.0 Flow data of USACE

The USACE carried out flow measurements using an ADCP at a number of transects in the St. Marys River as shown in the Google image in Fig.3. The yellow place-marks show the locations of these transects. There are five transects in the lower reach and the details of the velocity distribution in each of these five transects are described as follows:

Fig. 4 shows the contour plot of velocity variation in the cross-sectional plane for the transect 310. Transect 310 is just downstream of the Edison Sault Electric Company power plant tailrace. In Fig. 4, the higher ensemble number in the x-axis corresponds to Canadian side of the river and the lower ensemble number corresponds to the American side. In other words, the figure represents a view of the cross section as one would see when looking in the downstream direction. The flow depths near the left bank (Canadian side) are shallower (about 4 m range), whereas those near the right bank (American side) are deeper in the range of 8 to 9 metres. The river at this transect is about 800 metres wide. The figure shows that the velocity magnitudes in the centre portion of the river are higher in the range of 0.6 to 0.8 m/s, and the velocities near the banks are much lower near zero. In fact, there are flow reversals in these regions as can be seen from the "stick ship track" diagram shown in Fig. 5. The "stick ship track" diagram gives the relative position of the boat (red line) with the magnitude of average velocity vector represented as "sticks" (in blue). From Fig. 5, we can see that the flow in the central part of the river at this transect is predominantly in the longitudinal direction of the river. Only near the banks, there is some evidence of flow reversals. Zone of flow reversal on American side is larger than that on the Canadian side. The flow rate across this section at the time of measurement was 2030 m³/s.



Fig. 3. Google Earth image showing the ADCP transects (ADCP 310, ADCP 340, ADCP 330, ADCP 360 and ADCP 350as indicated by the yellow “place-marks”).

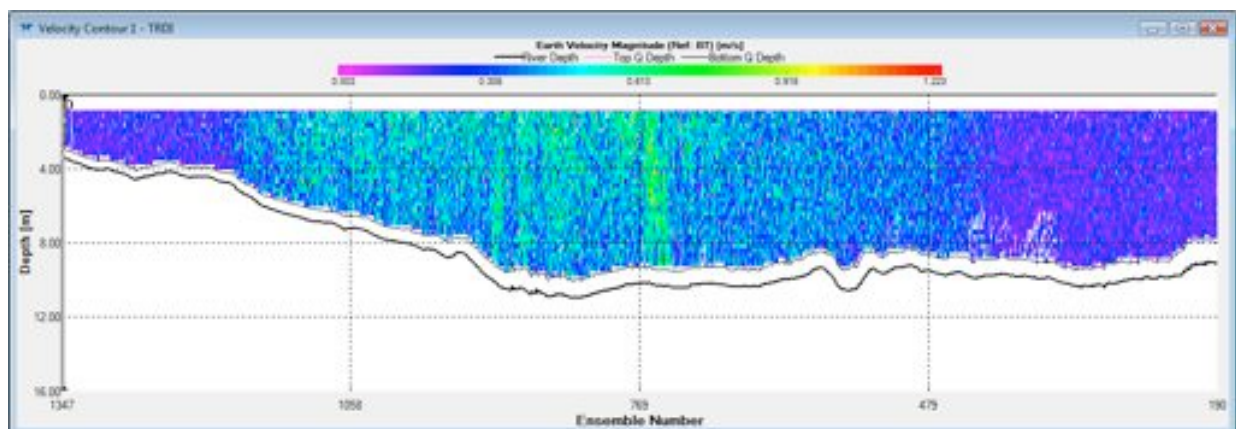


Fig. 4. Contour plot of magnitude of velocity vectors in the cross sectional plane across transect 310 (looking downstream).

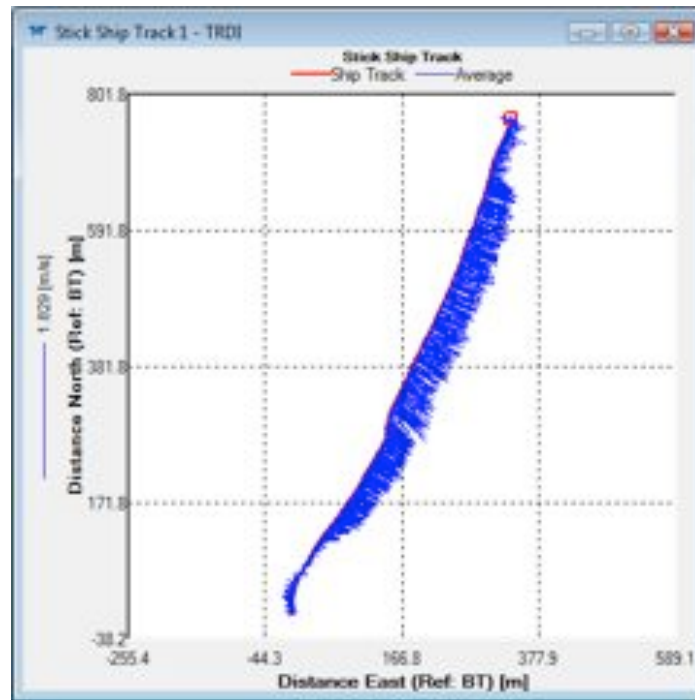


Fig. 5. "Stick ship track" diagram for transect 310.

Figs. 6 and 7 show the velocity contour and stick ship track diagram for transect 340. Transect 340 is about 475 metres downstream from Transect 310.

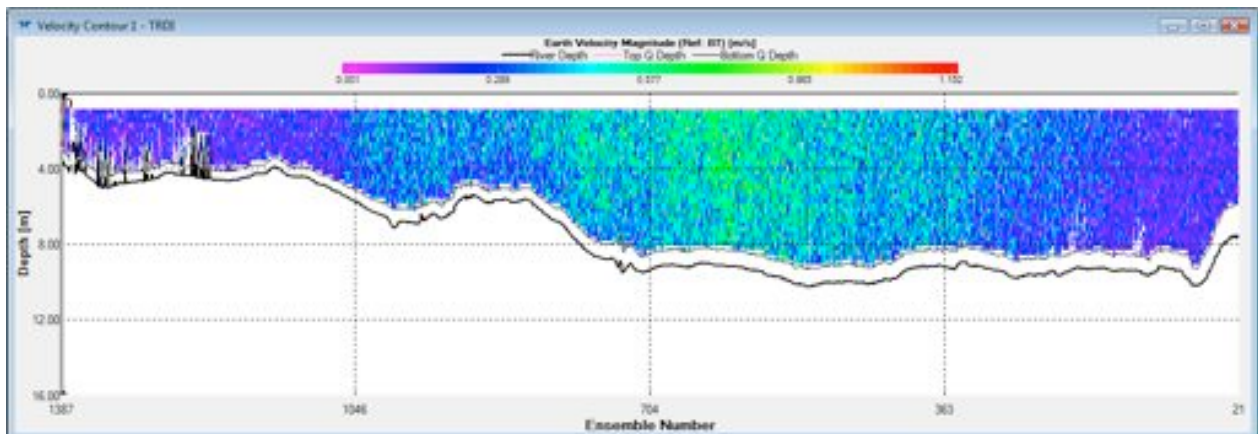


Fig. 6. Contour plot of magnitude of velocity vectors in the cross sectional plane across transect 340 (looking downstream).

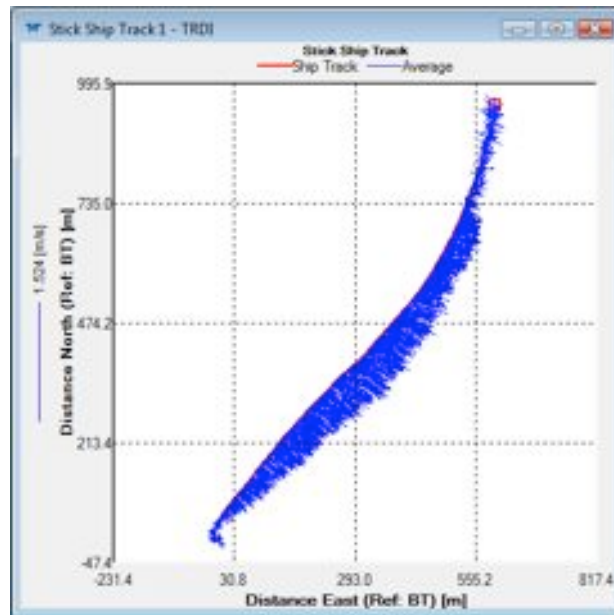


Fig. 7. "Stick ship track" diagram for transect 340.

From Figs. 6 and 7, we see that the flow depths and flow velocities in this transect are similar to transect 310 except for the river width, which at this transit is about 1100 m. At this transect, the flow reversal zone near the Canadian side is larger (about 200 m) compared to that near the American side (about 50 m). The flow rate at this transect at the time of measurement was $2350 \text{ m}^3/\text{s}$.

Figs. 8 and 9 show the velocity contour and the stick ship track diagram for transect 330, which is in the navigational branch of the St. Marys River near the entrance.

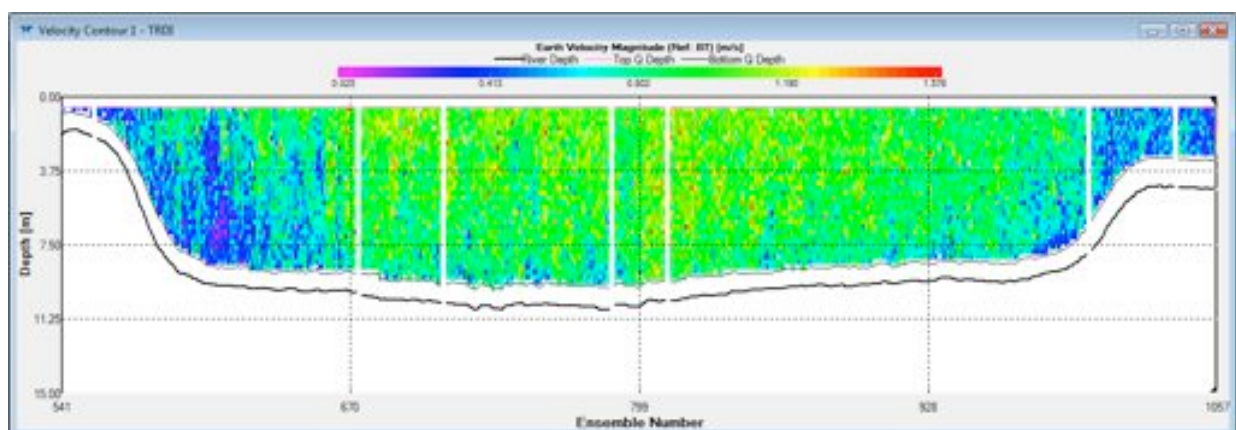


Fig. 8. Contour plot of magnitude of velocity vectors in the cross sectional plane across transect 330 in the Navigational channel (looking downstream).

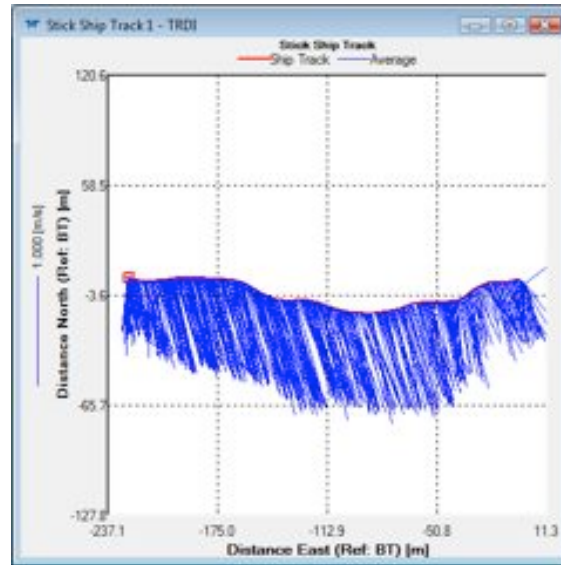


Fig. 9. “Stick ship track” diagram for transect 330

In Fig. 8, the left side of the figure corresponds to the river bank at the Sugar Island (East Bank) and the right side of the figure corresponds to the west bank of the river. The channel is about 200 metres wide and the velocities are much higher, and they are of the order of one metre per second in the central part of the river. Near the edges the velocities decrease to about 0.5 m/s. There are no flow-reversals at this transect and the flow is predominantly in the longitudinal direction of the channel. The flow rate through this transect at the time of measurement was about $1615 \text{ m}^3/\text{s}$.

Figs. 10 and 11 show the similar plots for transect 360. This transect is in the channel north of Sugar Island.

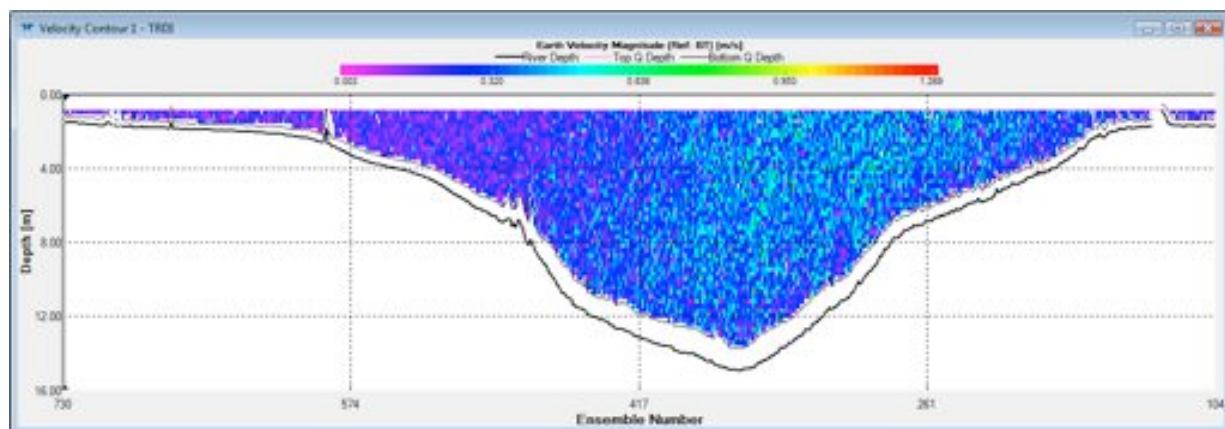


Fig. 10. Contour plot of magnitude of velocity vectors in the cross sectional plane across transect 360 in the channel north of Sugar Island (looking downstream).

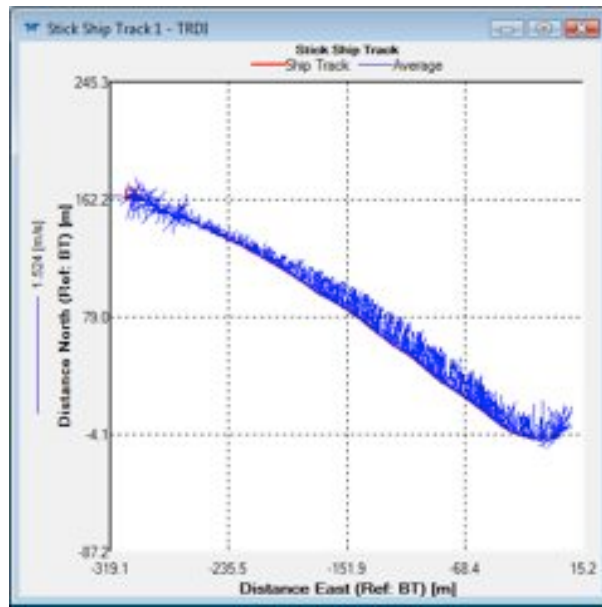


Fig. 11. “Stick ship track” diagram for transect 360.

From Fig. 10 and 11, we see that the flow velocities are considerably slower and they are of the order of 0.35 m/s in the central part of the river. The velocities near the banks are also much slower, and they are of the order of 0.10 m/s. The river at this site is about 300 metres wide and it is very shallow on either end and deeper in the middle. There is some evidence of flow reversals near the bank on the Canadian side. The flow rate through this section at the time of measurement was $588 \text{ m}^3/\text{s}$.

Figs. 12 and 13 give velocity and stick ship track diagram for Transect 350.

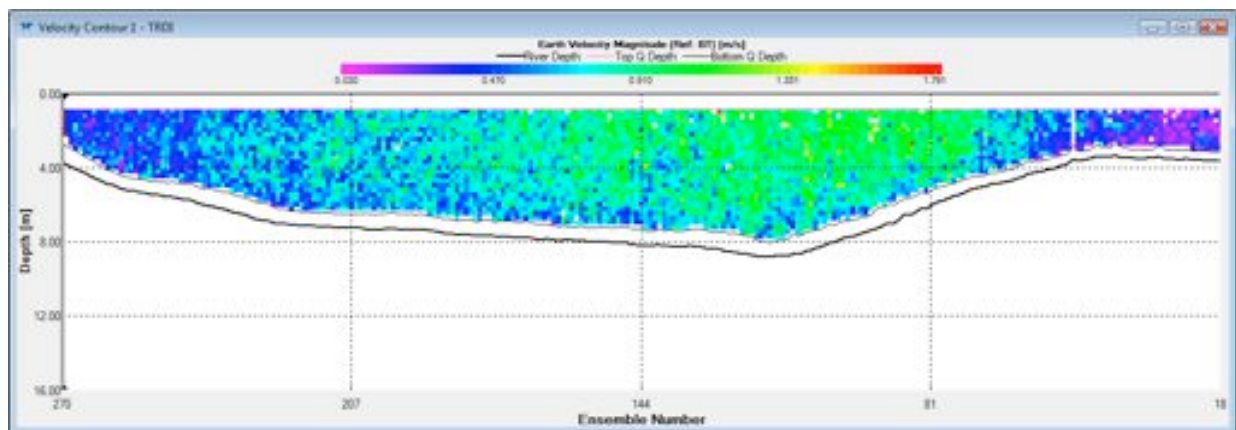


Fig. 12. Contour plot of magnitude of velocity vectors in the cross sectional plane across transect 350 in the channel downstream of Little Lake George (looking downstream).

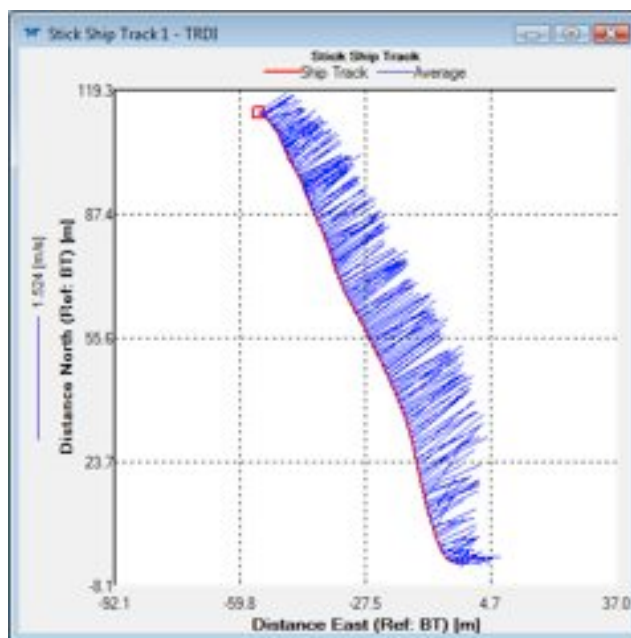


Fig. 13. “Stick ship track” diagram for transect 350.

The transect 350 is a narrow one. It is only about 120 metres wide. The flow velocities are comparatively higher, and they are in the order of 0.50 m/s. The flow velocities are aligned with the channel and there is no evidence of flow reversals at this transect. The flow rate measured at this transect was 605 m³/s.

From the flow data of USACE for the five transects in the St. Marys River, we can draw some general conclusions regarding the flow characteristics in this reach of the river. The flow is predominantly in the longitudinal direction in the central part of the river and the flow reversals are evident only near the edges at some part of the river. The flow cross sections show a large variation of flow depth across the river at all five transects, and the depth average flow velocities also vary substantially across the river in all of these transects. Consequently, the bed shear stress can be expected to vary across the river in this reach. The flow reversal zones can act as depositional zones for fine sediment transported by the flow from the upper river. Fine sediments enter the flow reversal zones because of transverse dispersion due to turbulence and advection due to transverse velocity component of the flow. Since fine sediments act as carriers for a number of contaminants, the deposited sediments are contaminated and an accumulation of the contaminated sediment occurs as a result of ongoing fine sediment deposition in these zones.

Fine sediments that do not get entrained in the flow reversal zones along the lengths of the river are transported downstream by the flow until they encounter low energy depositional areas such as Little Lake George and Lake George in the north branch and Lake Munuscong in

the navigational branch of the St. Marys River. The ADCP measurement show that the flow split in the navigational channel is 70% of the total flow. Therefore, bulk of the fine sediment load is expected to be transported through the navigational channel.

2.1. Selection of a flow and sediment transport model for the St. Marys River:

Since the variation of flow across the river is substantial, a one dimensional flow model may not be adequate for the reach of the river under consideration. Since the flow is predominantly in the longitudinal direction and the zones of flow reversals are not substantial, a three dimensional flow model may prove to be unnecessary. Therefore, a two dimensional flow and sediment transport model is deemed appropriate for this reach of the St. Marys River.

A two dimensional flow and sediment transport modelling system called TABS-MD with SMS user interface was selected for the St. Marys River in this study. The details of this modelling study including the description of the models, data requirements for implementation and calibration of the models, assessment of stability of contaminated sediment deposits to determine whether active sediment management action is required or not are described in this report.

3.0 Details of TABS-MD with SMS user interface

The modelling system TABS-MD consists of two model components, namely, RMA2 and RMA4. RMA2 is a two dimensional depth averaged finite element hydrodynamic model and RMA4 is a two dimensional depth averaged finite element sediment transport and water quality model. Both of these models were originally developed by Norton et al. (1973) for the United States Army Corps of Engineers. Subsequent enhancements to both of these models were made by researchers at the Resources Management Associates (RMA) and by the US ERDC WES Coastal and Hydraulics laboratory. Details of the current versions of both RMA2 and RMA4 models can be found in Donnell et al. (2008) and Letter et al. (2008) respectively. Some of the salient features of these two models are given here for the sake of completeness.

3.1 RMA2 Model:

RMA2 model solves the Reynolds form of the Navier-Stokes equation for turbulent flows using finite element method. It computes water surface elevations and the depth averaged horizontal velocity components for subcritical, free surface two-dimensional flow fields. The governing equations solved in the model are as follows:

$$h \frac{\partial u}{\partial t} + hu \frac{\partial u}{\partial x} + hv \frac{\partial u}{\partial y} - \frac{h}{\rho} \left[E_{xx} \frac{\partial^2 u}{\partial x^2} + E_{xy} \frac{\partial^2 u}{\partial y^2} \right] + gh \left[\frac{\partial a}{\partial x} + \frac{\partial h}{\partial x} \right] + \frac{gun^2}{\left(1.486h^{\frac{1}{6}}\right)^2} (u^2 + v^2)^{\frac{1}{2}} - \zeta V_a^2 \cos\psi - 2hv\omega \sin\Phi = 0 \quad (1)$$

$$h \frac{\partial v}{\partial t} + hu \frac{\partial v}{\partial x} + hv \frac{\partial v}{\partial y} - \frac{h}{\rho} \left[E_{yx} \frac{\partial^2 v}{\partial x^2} + E_{yy} \frac{\partial^2 v}{\partial y^2} \right] + gh \left[\frac{\partial a}{\partial y} + \frac{\partial h}{\partial y} \right] + \frac{gvn^2}{\left(1.486h^{\frac{1}{6}}\right)^2} (u^2 + v^2)^{\frac{1}{2}} - \zeta V_a^2 \sin\psi - 2hu\omega \sin\Phi = 0 \quad (2)$$

$$\frac{\partial h}{\partial t} + h \left(\frac{\partial u}{\partial x} + \frac{\partial v}{\partial y} \right) + u \frac{\partial h}{\partial x} + v \frac{\partial h}{\partial y} = 0 \quad (3)$$

where

h = water depth

u, v = velocity components in the horizontal plane (x and y directions respectively)

x, y, t = Cartesian coordinates and time

ρ = density of fluid

E = eddy viscosity coefficient

subscript xx = normal direction on x axis surface

subscript yy = normal direction on y axis surface

subscript xy and yx = shear directions on each surface

g = acceleration due to gravity

a = bottom elevation

n = Manning's roughness coefficient

ζ = empirical wind shear coefficient

V_a = wind speed

Ψ = wind direction

ω = rate of earth's angular rotation

Φ = local latitude

In RMA2 model, the governing equations are solved by the finite element method using the Galerkin Method of weighted residuals. The elements may be one-dimensional channel reaches, or two-dimensional quadrilaterals or triangles, and may have curved (parabolic) sides. The shape (basis) functions are quadratic for velocity and linear for depth. Integration in space is performed by Gaussian integration. The solution is fully implicit and the set of simultaneous equations is solved by Newton-Raphson non-linear iteration scheme. From the solution of the model, the bed shear stresses can be calculated as follows:

$$\tau_x = \rho g \left(\frac{n}{1.486} \right)^2 \frac{u \sqrt{u^2 + v^2}}{h^{\frac{1}{3}}} \quad (4)$$

$$\tau_y = \rho g \left(\frac{n}{1.486} \right)^2 \frac{v \sqrt{u^2 + v^2}}{h^{\frac{1}{3}}} \quad (5)$$

where τ_x and τ_y are bed shear stresses along the x and y coordinate directions respectively. For further details of the model, the user manual by Dunnell et al. (2008) can be consulted.

3.2 RMA4 Model:

RMA4 model solves the depth averaged mass balance equation taking into account advection, dispersion, first order decay and source and sink. It computes concentrations for up to six constituents, either conservative or non-conservative, within the one and/or two dimensional computational mesh domain. The form of the governing equation solved in the model is as follows:

$$h \left(\frac{\partial c}{\partial t} + u \frac{\partial c}{\partial x} + v \frac{\partial c}{\partial y} - \frac{\partial}{\partial x} D_x \frac{\partial c}{\partial x} - \frac{\partial}{\partial y} D_y \frac{\partial c}{\partial y} - \sigma + kc + \frac{R_c}{h} \right) = 0 \quad (6)$$

where

h, u, v, t, x, y = parameters defined in RMA2 model.

c = concentration of a substance undergoing transport and mixing

D_x and D_y = dispersion coefficients in x and y directions respectively

k = first order decay rate

σ = source/sink rate of substance

R_c = rainfall/evaporation rate.

The above governing equation is also valid for the treatment of sediment transport. The difference is in the specification of the source sink term. With appropriate specification of the source sink term, the RMA4 model can be used to treat the transport of sediment in the flow.

In RMA4, the above equation was solved by the finite element method using Galerkin weighted residuals. As with RMA2, the RMA4 model handles one-dimensional segments or two-dimensional quadrilaterals or triangles. Curved element edges are also supported. Spatial integration of the equations was performed by Gaussian techniques and the temporal variations are handled by nonlinear finite differences consistent with the method for RMA2. Both RMA2 and RMA4 models are fully integrated by a user interface called SMS. The hydrodynamic solution of RMA2 is imported into RMA4 to provide the velocity field which is driving force for the mixing process represented in RMA4 model. Complete details of the model can be found in Letter et al. (2008).

3.3 SMS User Interface:

SMS is a graphical pre-and post processor for numerical surface water models and it allows for interactive editing and display of finite element networks. Display controls allow the user to adjust colour and line contouring to display either bed elevations or model results such as velocity fields and water surface elevations. SMS consists of several modules. A data module manages scattered data sets and digital elevation models, and it includes tools for performing data analysis and interpretation. A mapping module allows the user to create a conceptual model and use background images to interface with the finite element mesh of the computational domain. A mesh module allows the creation of finite element meshes for different hydrodynamic modelling systems. SMS is a proprietary model and it is being supported by AQUAVEO (www.aquaveo.com). The most recent version of SMS (SMS Version 10.1) is used in this study.

4.0 Modelling domain and geometry data

The river reach selected for modelling is shown in Fig. 14. The length of the reach modelled is about 12.5 km. The modelled reach begins at the foot of the rapids and extends up to Little George Lake on the main river. A portion of the navigational channel near the channel entrance is also included in the modelling domain.

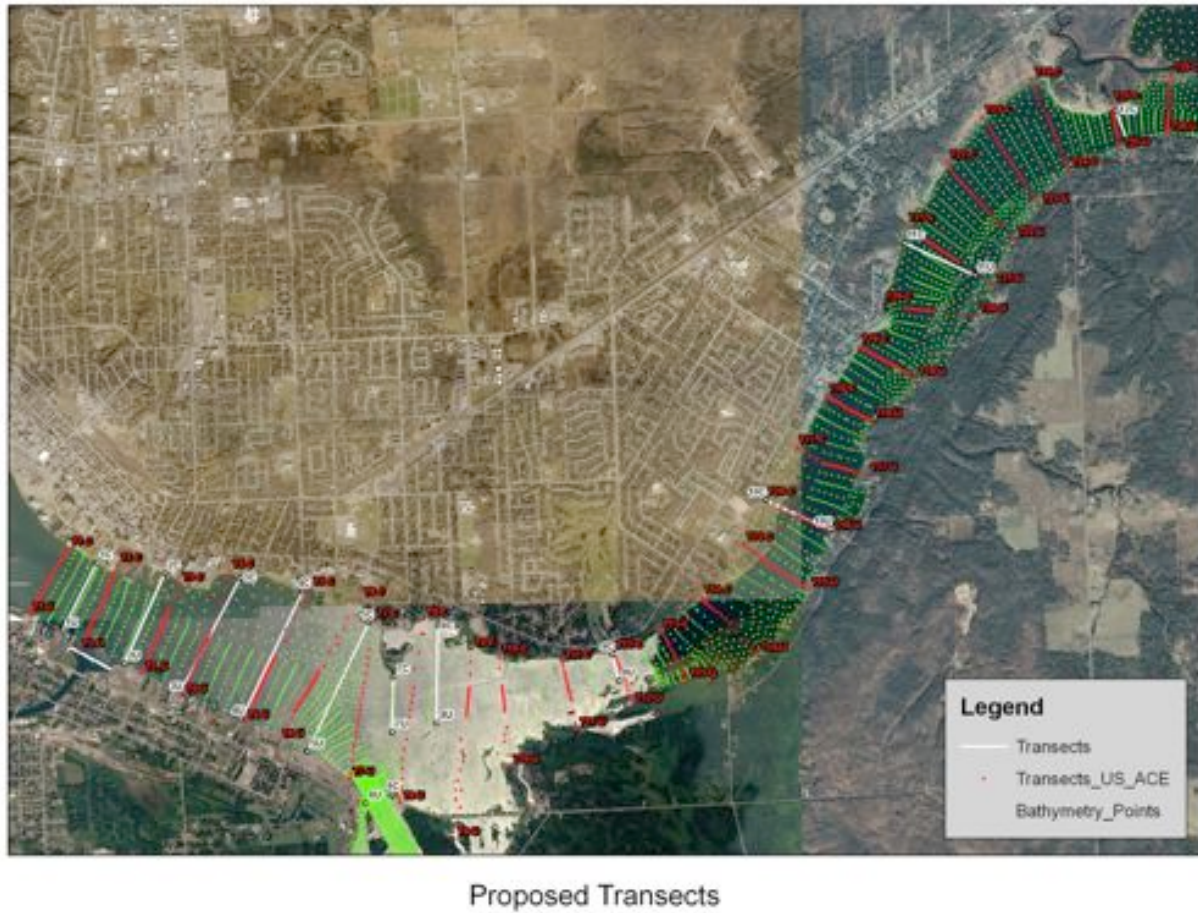


Fig. 14. River reach selected as modelling domain with bathymetry data (shown as green points).

The bathymetry data for the selected reach was obtained from USACE Detroit district office (Eric Tauriainen). The coverage of the bathymetry data is shown in Fig. 14 as green points. The bathymetry points were imported into SMS model and a fine grid finite element mesh was generated as shown in Fig.15.

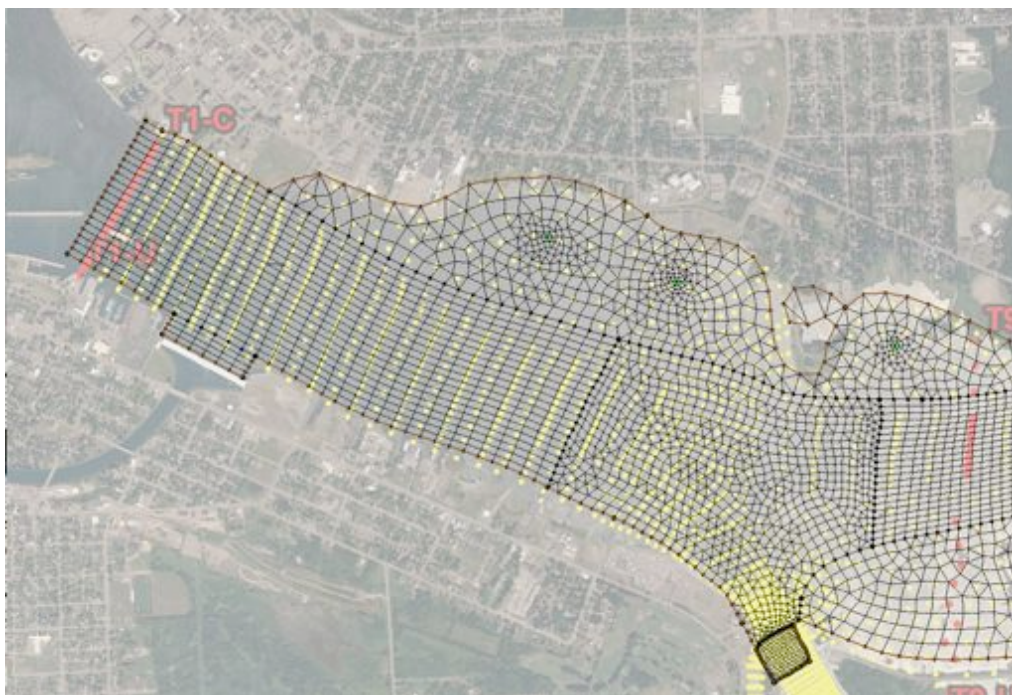


Fig. 15a Upper part of the finite element mesh generated using SMS.



Fig.15b. Middle part of the finite element grid generated using SMS.



Fig. 15c. The lower part of the finite element mesh generated using SMS.

SMS model allows for dividing the computational domain into polygons where the flow properties such as bed roughness and turbulence characteristics can be considered as homogeneous. These polygons also facilitate the development of the meshes appropriate for the flow conditions that is likely to exist in different part of the flow region. In the present development of the model, thirteen such polygons were used. Eight of these polygons contain rectangular elements and the remaining five polygons contain triangular elements. The total number of elements generated was 6113, out of which 4926 are rectangular elements and 1187 are triangular elements. The total number of nodal points where the flow properties are computed is 17600, and the number of resulting algebraic equations is 52800.

5.0 Specification of boundary conditions:

Boundary conditions have to be specified to the modelling domain to solve the flow field. Normally, the RMA2 model requires a flow rate boundary condition at the upstream boundary and a water surface elevation boundary condition at the downstream boundary. For the present model, the flow rate for the upstream boundary was obtained from the Environment Canada Great Lakes-St. Lawrence River Regulation Office (Rob Caldwell). The flow rate was split into two components, one entering the river at the upstream boundary and the other entering the Edison Sault Hydro Electric Power plant. Monthly average data was used for the model.

The total monthly flow rate, which includes the power plant flow for the period from 1900 to 2009 is plotted in Fig. 16 as a function of time for the different months. The average flow rate for the period of record is $2120 \text{ m}^3/\text{sec}$. The maximum flow rate is $3740 \text{ m}^3/\text{sec}$, which occurred during the month of November in 1985. The minimum flow rate for the period of record is $1160 \text{ m}^3/\text{sec}$ and it occurred in September of 1955.

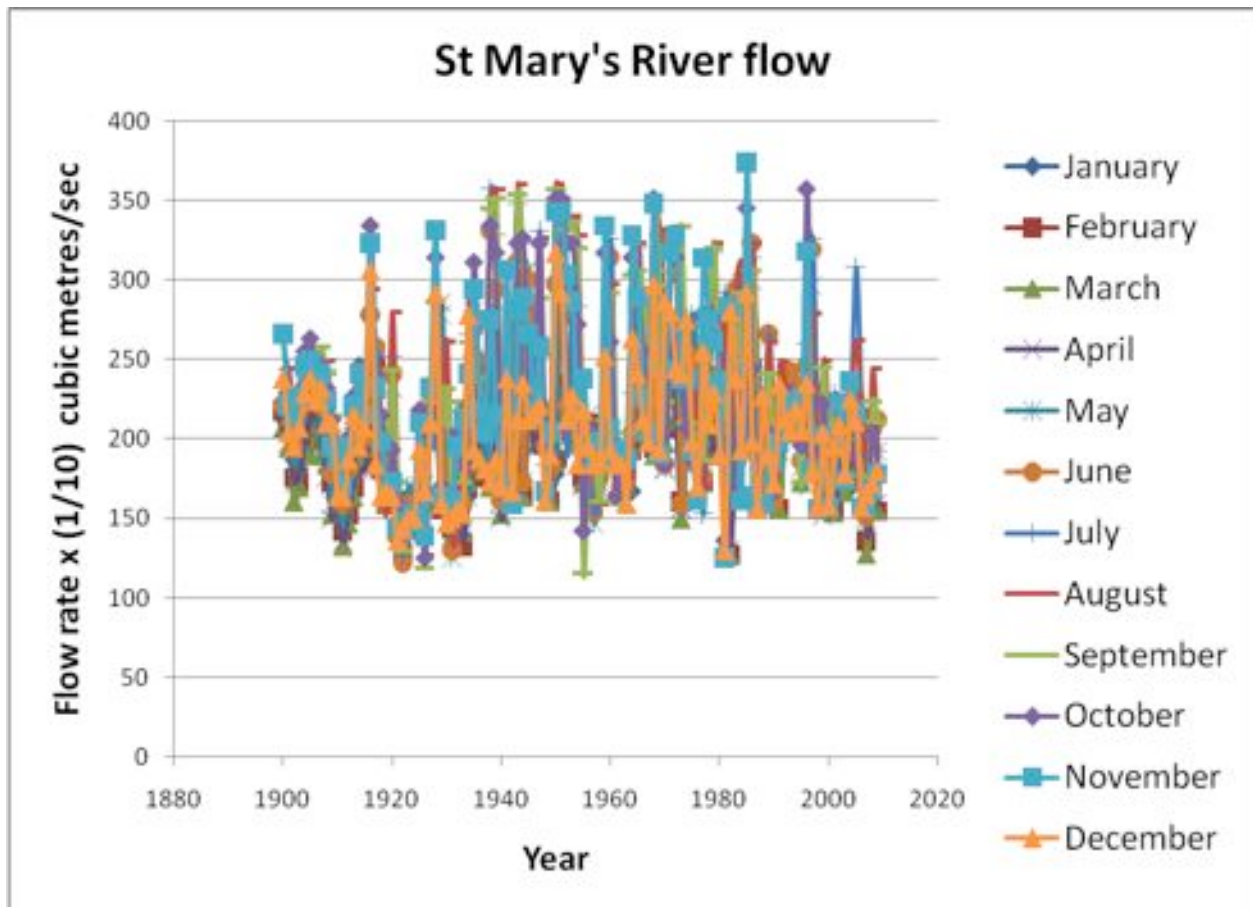


Fig. 16. Monthly average flow rate for the St. Marys River (Source: Environment Canada, Great Lakes-St. Lawrence River Regulation Office).

The flow rate through the Edison Sault Electric Company for the period from 1983 to 2009 is shown in Fig. 17. In this figure, monthly average values are plotted as a function of time for various months. The average flow rate over a period of 27 years is $576 \text{ m}^3/\text{sec}$. The maximum flow rate is $867 \text{ m}^3/\text{sec}$ (1985 September) and the minimum flow rate is $135 \text{ m}^3/\text{sec}$ (1983 September) for the period of record.

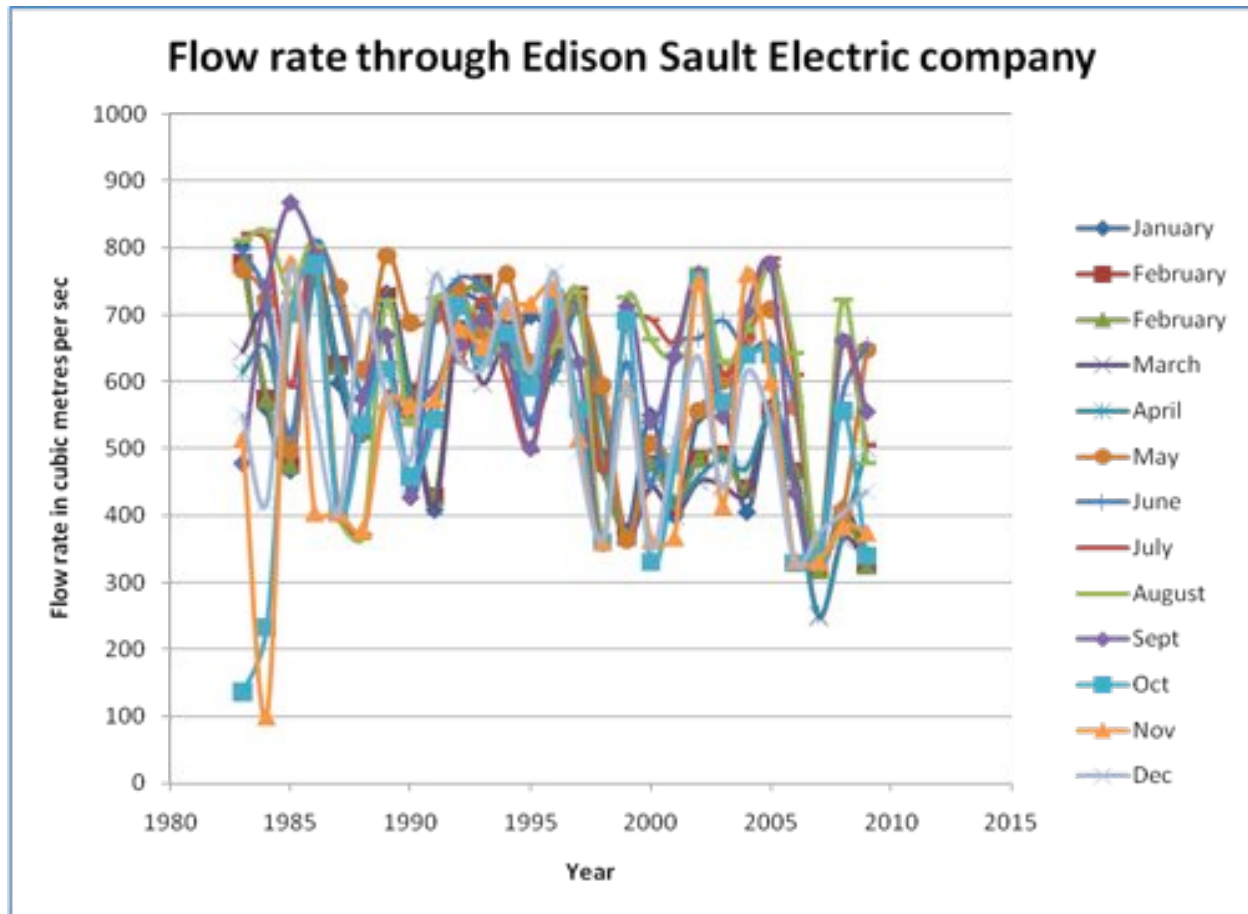


Fig. 17. Monthly average flow rate through Edison Sault Electric company power plant.

Two more boundary conditions need to be specified for the present model: One for the boundary in the navigational channel and the other for the boundary at the downstream end of the computational domain in the main river. Neither the flow rate data nor the water surface elevation data is available for these two boundaries. Therefore, a nested modelling approach is used in the present study. Accordingly, a coarse grid, RMA2 model developed by USACE for the entire St. Marys River is used to solve for flow and water surface elevation at the boundaries of the present fine grid model. The USACE developed this coarse grid model in 2003 to investigate the impact of a proposed dredging project on water levels and flows in the St. Marys River (Aaron Thompson). The coverage of the model is shown in Fig. 18. The boundary conditions used for the model are as follows: For the upstream boundary, the monthly average flow rate data of Environment Canada Great Lakes- St. Lawrence River Regulation Office was used as is done for the present fine grid model. For the downstream boundaries, the flow stages measured at Thessalon, Slab Dock and Rock Cut Channel gauging stations in the St. Marys River system were used. Since the objective of the model is to predict the flow rate and water levels for the entire river, the elements used in this model are coarse and hence the model is not

suitable for predicting the finer flow details such as flow reversals and re-circulating eddies. The present fine grid model, on the other hand, focuses on a much shorter reach (12.5 km) and uses a much finer mesh and hence is capable of predicting such finer details of the flow field.

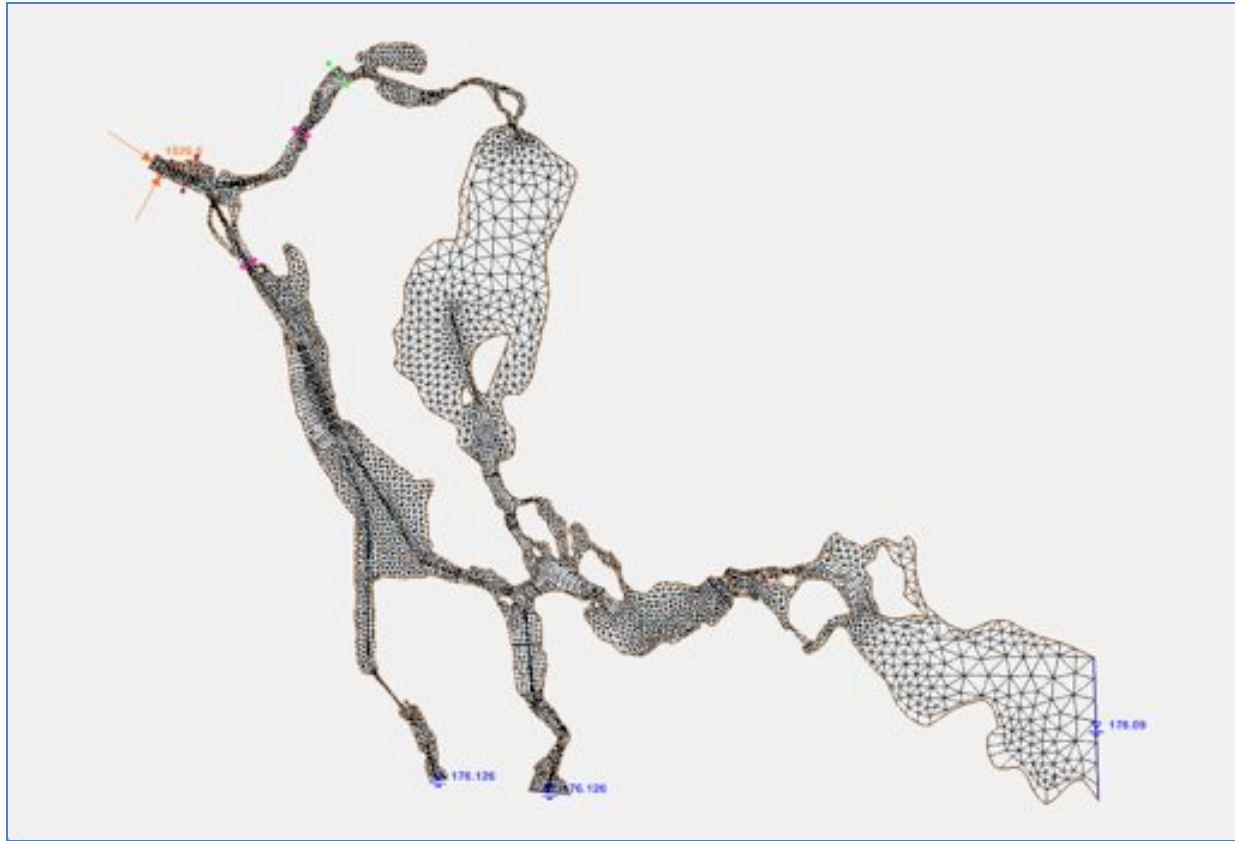


Fig. 18. Coverage of the coarse grid RMA2 model developed by USACE for the entire St. Marys River system (Eric Tauriainen).

6.0 Calibration of the model

Calibration of the present model was carried out by adjusting the roughness parameter (Manning's n) and the eddy viscosity coefficient and comparing the predicted velocity distributions with the ADCP data presented earlier. A typical comparison between the model predictions and measured ADCP data for one of the transects is shown in Fig. 19. It can be seen from this figure that the predicted magnitude and direction of the depth average velocities agree reasonably well with the data. Selection of the Manning's n values for the river was guided by the images of the river bed collected using an underwater video camera by

Environment Canada (Hans Biberhofer). The eddy viscosity values used for the model are well within the range of values recommended in the user manual (Dunnell et al. (2008)).

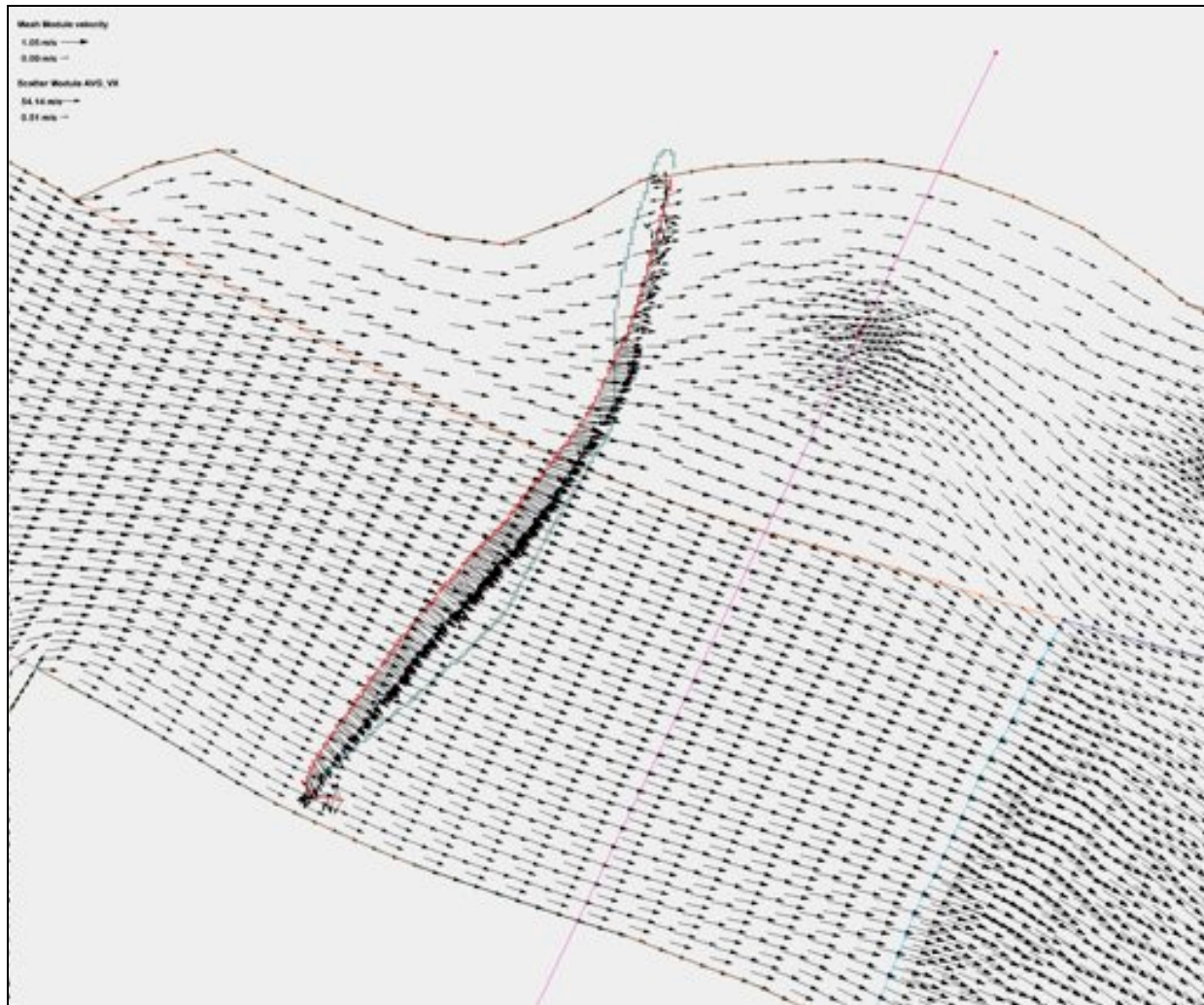


Fig. 19. A typical agreement between the model prediction and the ADCP data measured in one of the transects in the St. Marys River.

7.0 Results from the model simulations

Model simulations were carried out for maximum, minimum and average flow conditions (also referred to as high, low and mean flow respectively) that existed in the river for over a period of one hundred and ten years. The results of the simulation for the average flow condition are presented here. The results of simulation for maximum and minimum flows are presented in Appendix A. For the average flow conditions, the model was run for an upstream flow rate of 2120 m³/sec. This flow rate was split into two parts: one entering the flow domain from the

upper river and the other entering the river from the power plant. The average flow through the power plant is $576 \text{ m}^3/\text{sec}$ (27 year average), and therefore, flow from the upper the river becomes $1544 \text{ m}^3/\text{sec}$. The flow rate boundary conditions at the navigational channel and the water surface elevation boundary condition at the downstream boundary of the lower main river were obtained by running the coarse grid model of USACE. The values computed were as follows: Navigation channel flow rate is equal to $1560 \text{ m}^3/\text{sec}$, and the water surface elevation at the downstream boundary is equal to 176.75 m. The model was run with these boundary conditions, and the results from the model are depicted in the following figures 20 to 28. Fig. 20a shows the velocity vectors computed for the upper part of the computational domain. Fig. 20 b and c show the flow velocities for the middle and lower parts respectively.

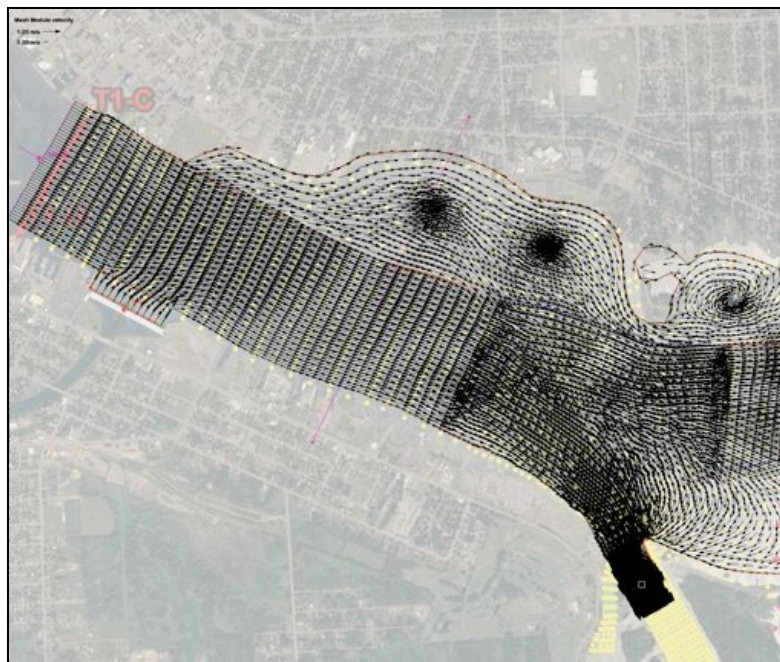


Fig. 20 a. Velocity vectors predicted by the model for the upper part of the flow domain.

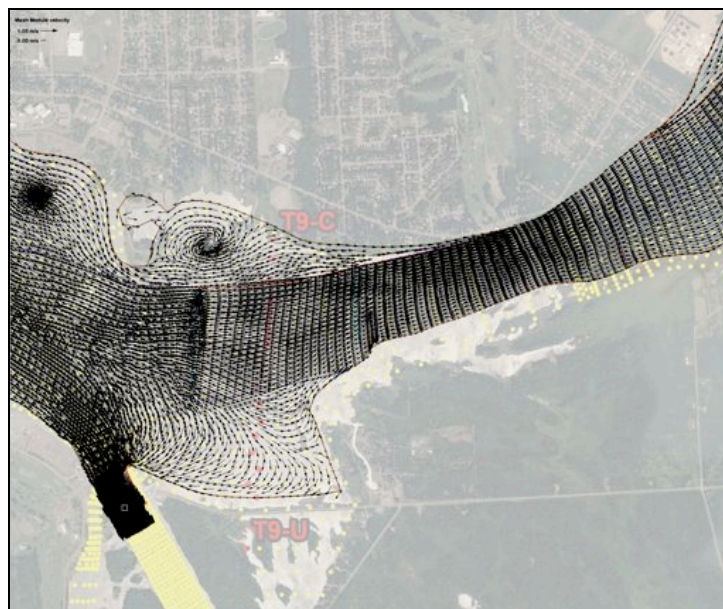


Fig. 20b. Velocity vectors predicted by the model for the middle part of the flow domain.



Fig. 20c. Velocity vectors predicted by the model for the lower part of the flow domain.

Fig. 21 shows the magnitude of flow velocities over the computational domain. We can see from this figure that the flow velocities are higher in the middle of the river (light blue) and also in the navigational channel (yellow). There are areas of low velocities shown in dark blue where the deposition of fine sediment is likely to occur.



Fig. 21. Computed magnitude of flow velocities in the computational domain for average flow conditions.

Fig. 22 shows the flow depth variation over the computational domain. The river is deeper in the upper part and also in the navigational channel (shown in blue). There are some deeper portions in the lower river as well. There is a large portion of the river along the river banks in the lower part, where the water depth is shallow (shown in orange).

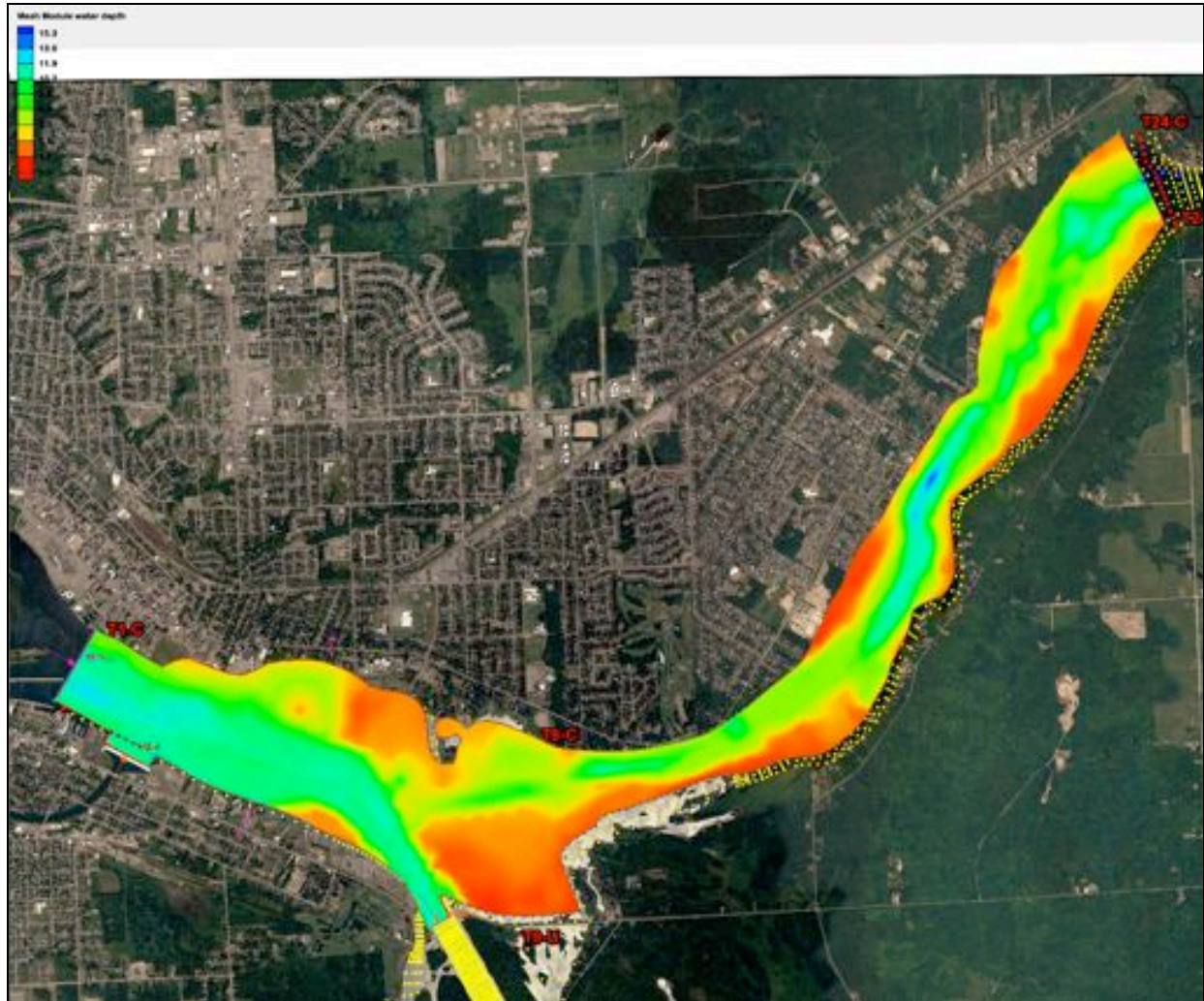


Fig.22. Computed flow depths over the computational flow domain for average flow condition.

Fig.23 shows the water surface elevations computed by the model for the river reach modelled. The water surface elevations are higher in the upstream regions (shown in dark orange) and they decrease in the downstream direction as one would expect (shown in light yellow). The water level drop between upper stream and downstream sections is in the range of three to four cm.



Fig. 23. Computed water surface elevations over the computational domain for the average flow condition.

Fig. 24 displays the computed bed shear stress distributions over the computational domain. The lower values are represented by the deep blue colour. The bed shear stress values are larger at the centre of the river and also at the navigational channel. The computed shear stress distributions will be used to assess the stability of the contaminated sediment.

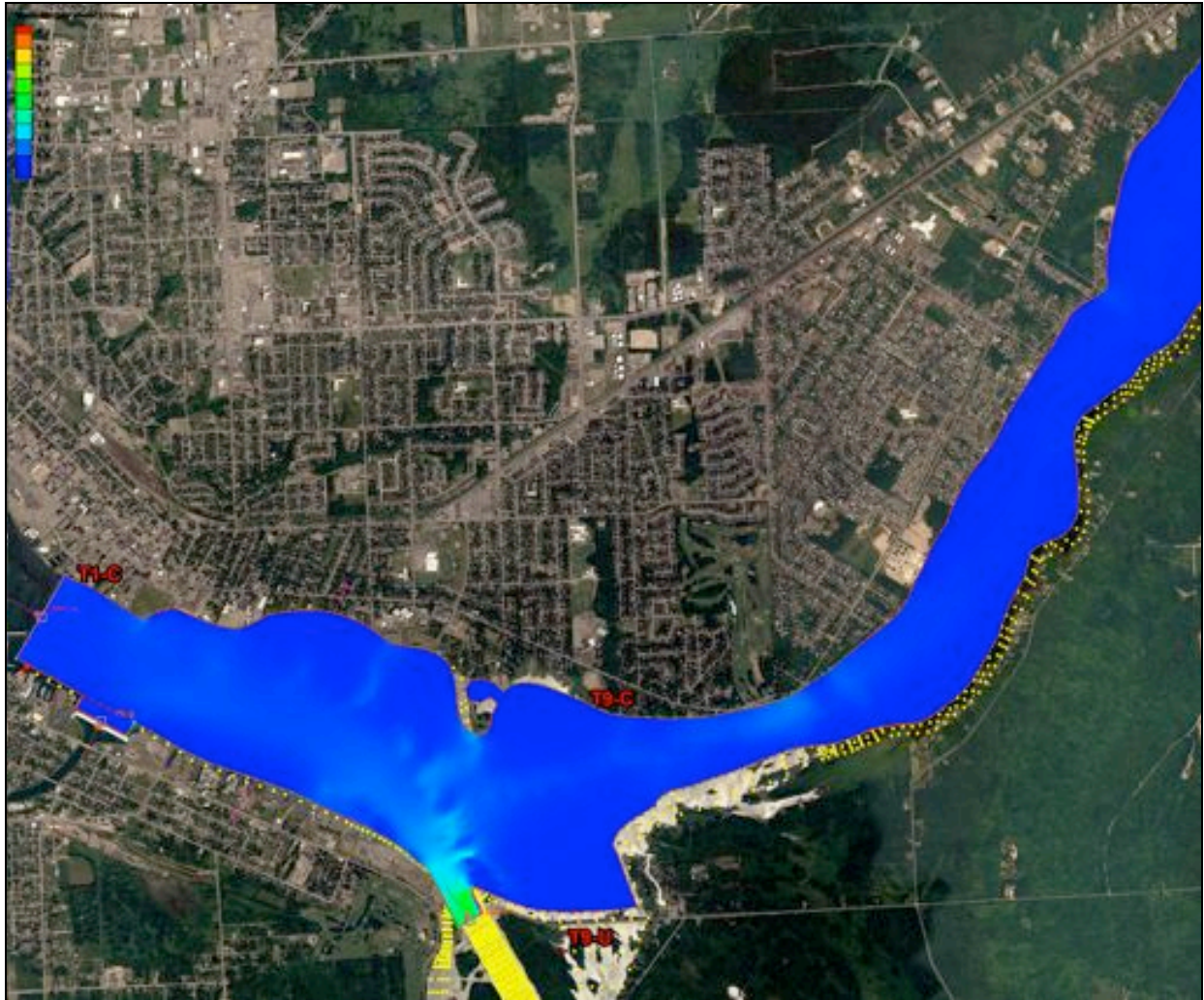


Fig. 24. Computed bed shear stress distribution over the computational domain for average flow condition.

0.30

0.25

0.20

0.15

0.10

Transect ,

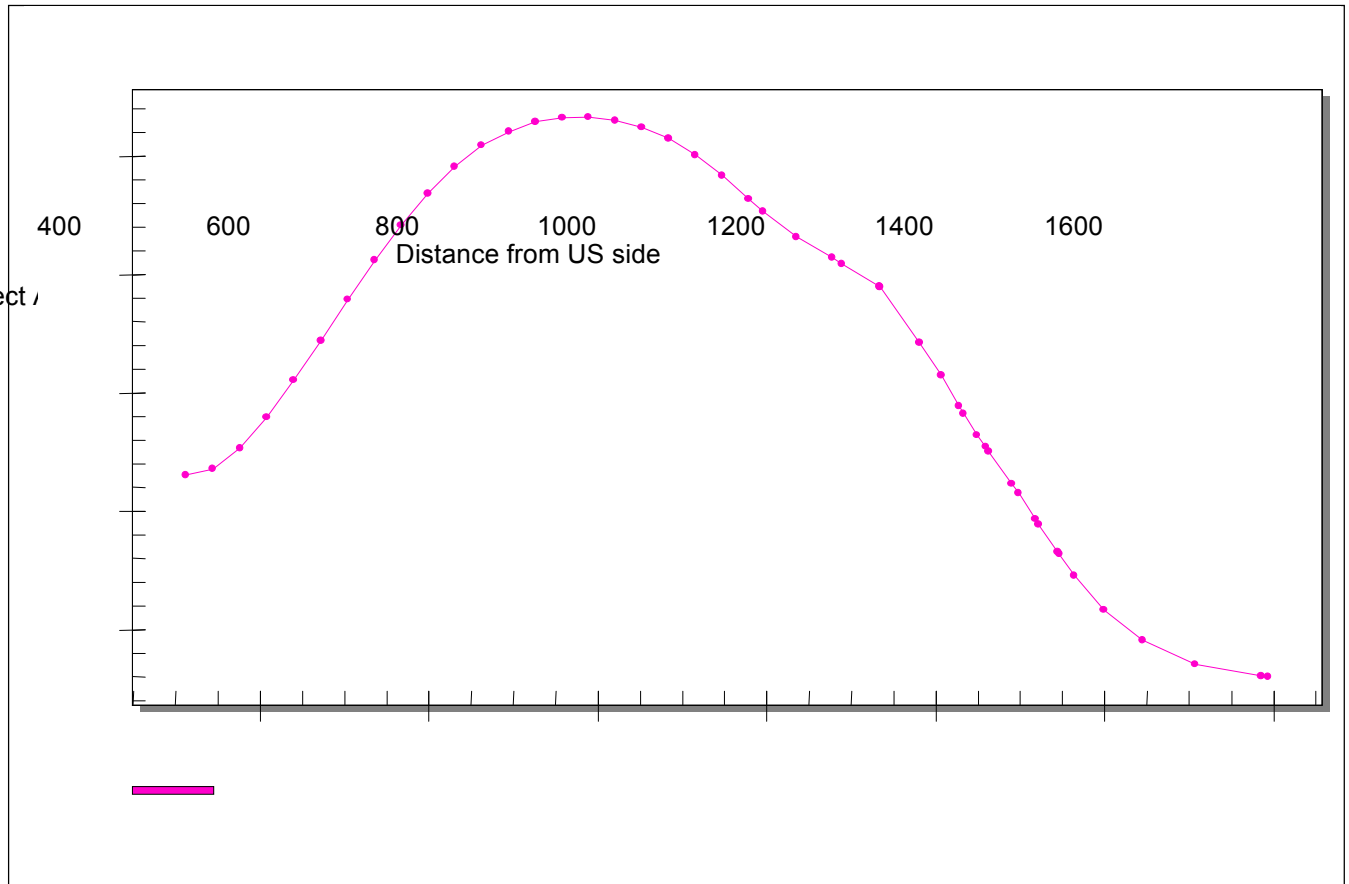


Fig. 25. Variation of simulated velocity magnitudes across the upper part of the Lower St. Marys River.

Fig. 26 shows the variation of the bed shear stress across the river in the upper part of the computational domain for the average flow condition. The magnitudes of the bed shear stresses in the central portion of the river are in the range of 0.40 to 0.45 Pa and they decrease to very low values in the range of 0.02 to 0.03 near the banks. The knowledge of the bed shear stress magnitudes is crucial for assessing the stability of sediment on the river bed.

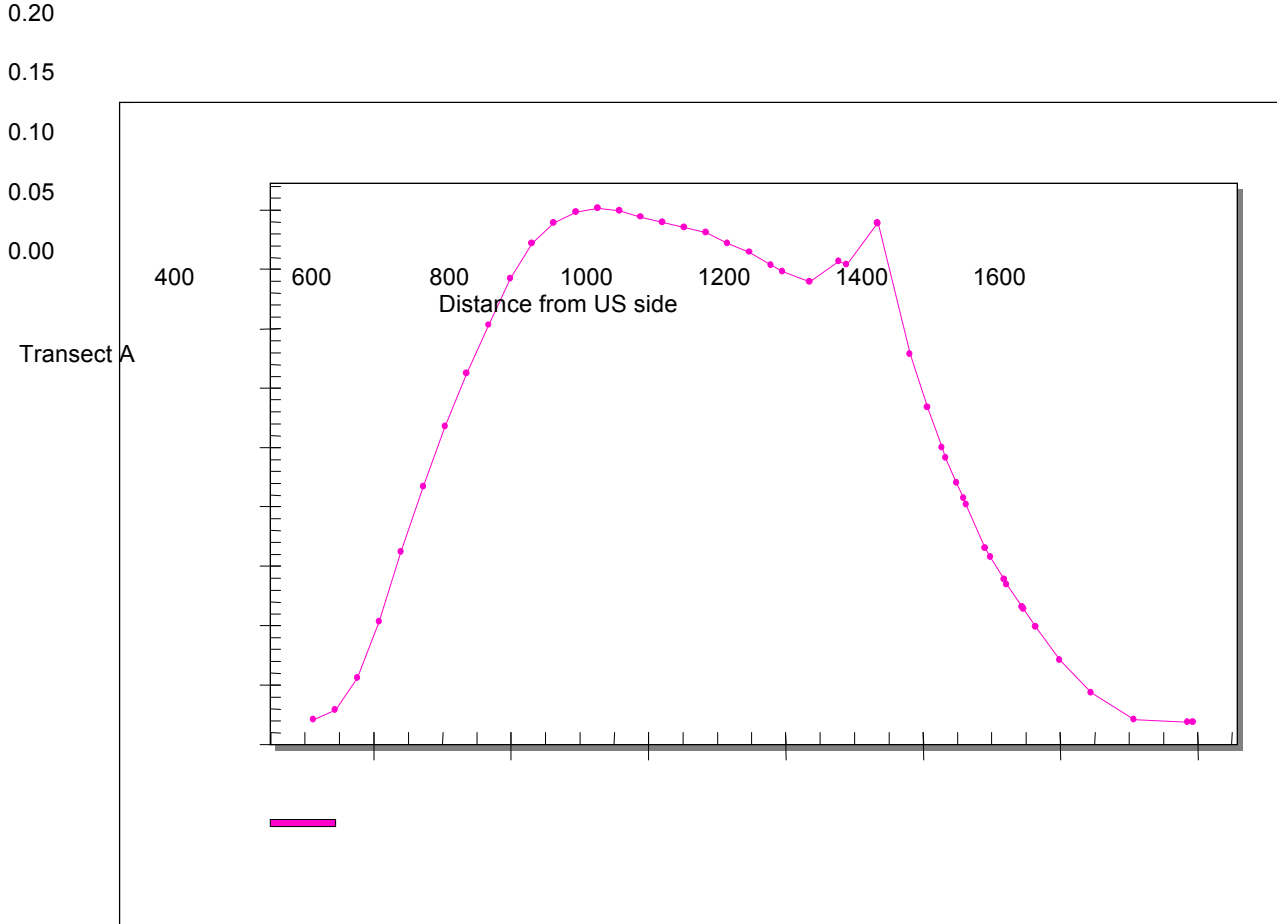


Fig. 26. Bed shear stress variation across a section in the upper part of the lower St. Marys River.

A comparison of the velocity magnitudes predicted by the model for different flow conditions is shown in Fig. 27. In this figure, the square points represent the maximum flow condition, the diamond points represent the minimum flow condition and the filled circles represent the average flow condition. From this figure, we can see that the velocity magnitudes are almost double the values corresponding to average flow conditions. At low flow condition, the velocity magnitudes are about half the values corresponding to the average flow condition. The distribution of the velocity magnitude across the river is fairly similar for all three flow conditions.

0.5

0.4

0.3

0.2

0.1

400

600

800

1000

Distance from US side

1200

1400

1600

stmarys_river_revised_test1.sol (RMA2), velocity mag

stmarys_river_revised_test2.sol (RMA2), velocity mag

stmarys_river_revised_test3.sol (RMA2), velocity mag

Transect A



Fig. 27. Comparison of velocity magnitude different flow conditions as predicted by the model.

A comparison of the bed shear stresses for different flow conditions as predicted by the model is shown in Fig. 28. The legend used for this figure is same as that used in Fig. 27. From this figure, we can see that for maximum flow condition, the bed shear stress values are about four times larger than those for the average flow condition. For the low flows, bed shear stress values are about half of the values corresponding to the average flow condition. The bed shear stress values predicted by the model are useful to assess the stability of sediment in the St. Marys River.

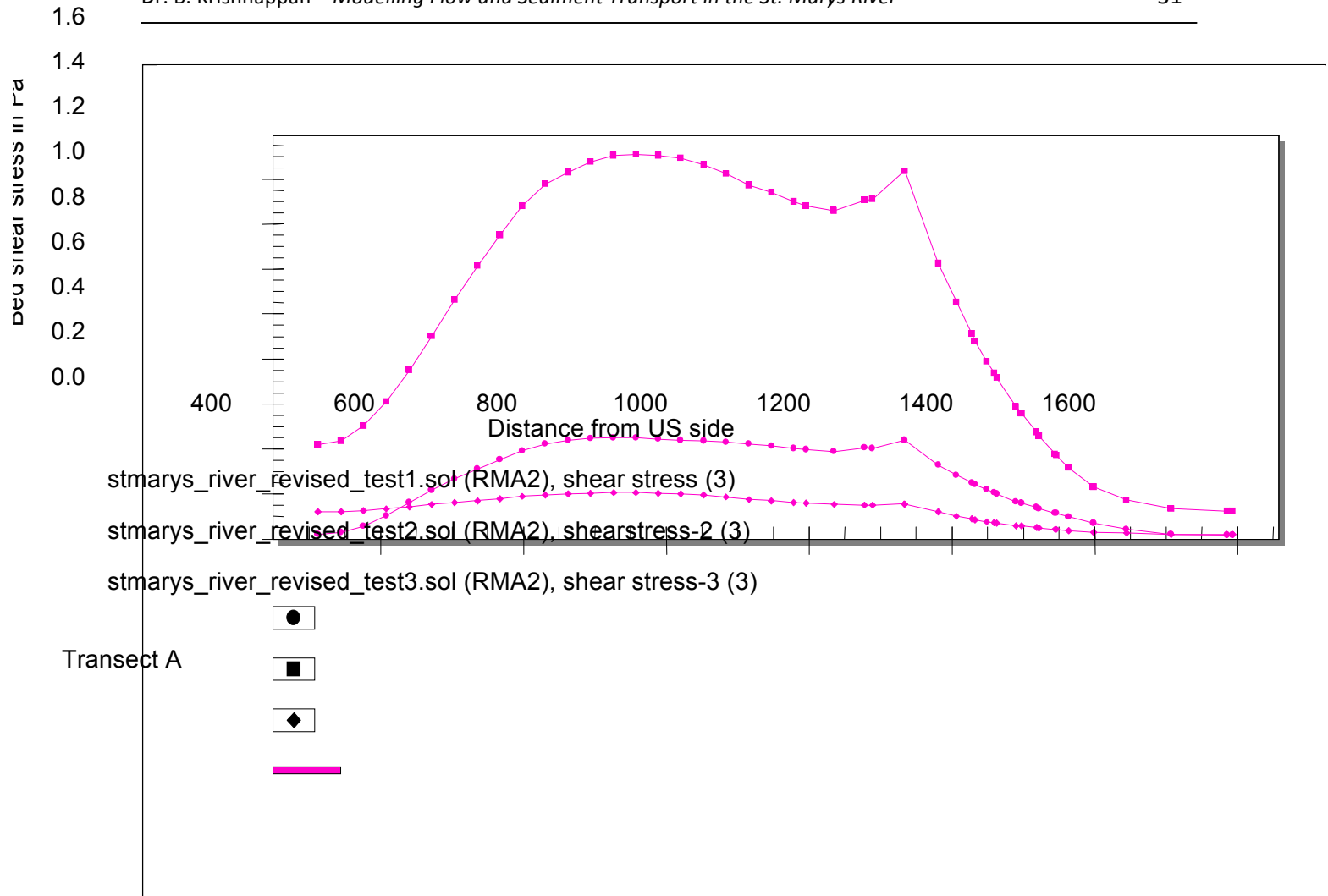


Fig. 28. Comparison of bed shear stresses for different flow conditions as predicted by the model.

8.0 Assessment of stability of sediment deposits

The assessment of stability of sediment deposits in St. Marys River requires knowledge of both bed shear stress as well as sediment characteristics including the critical shear stress for erosion of the deposited sediment. Sediment characteristics including the critical shear stress for erosion were obtained from a field study that was undertaken by Environment Canada's National Water Research Institute in Burlington, Ontario (Hans Biberhofer). Details of this study are as follows:

8.1 Video Imaging of the river bed:

Nature of the sediment forming the bed of the St. Marys River was examined by carrying out a video imaging study in the modelled river reach. The video imaging system used in the study consists of an under- water video camera mounted on a fish weight, which is towed in the river from a boat. The camera is pointed down and it is focused on the tail end of the fish weight. A depth gauge and a thermometer were also incorporated in this video system. A GPS system provides the positioning of measurement stations. A photograph of the system used in this study is shown in Fig. 29.

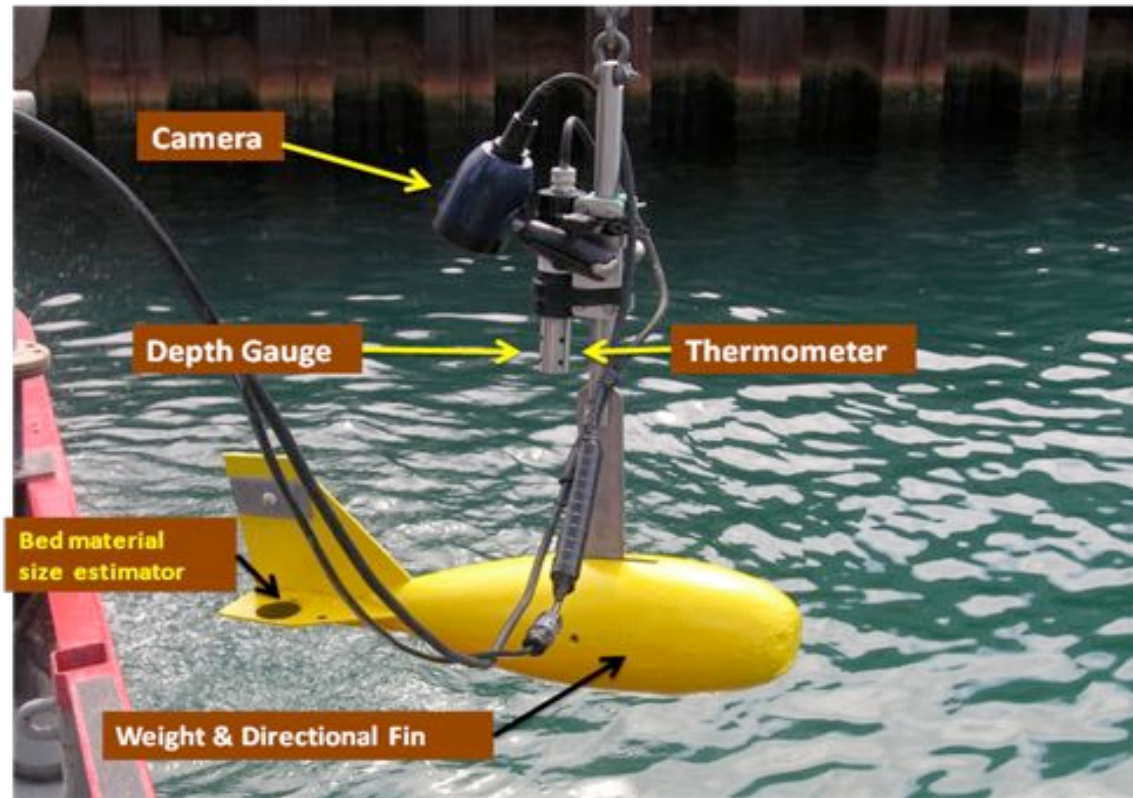


Fig. 29. Video Imaging system developed by Environment Canada (Hans Biberhofer)

To provide scaling for the images, two filled circles (5 cm and 4 cm in diameter) were drawn on one side and a 2 cm x 2 cm cross on the opposite side of the fin of the fish weight. The video imaging system was deployed from a boat and the boat was traversed along a number of transects in the river. The locations of the transects are shown in Fig. 30 as yellow lines.

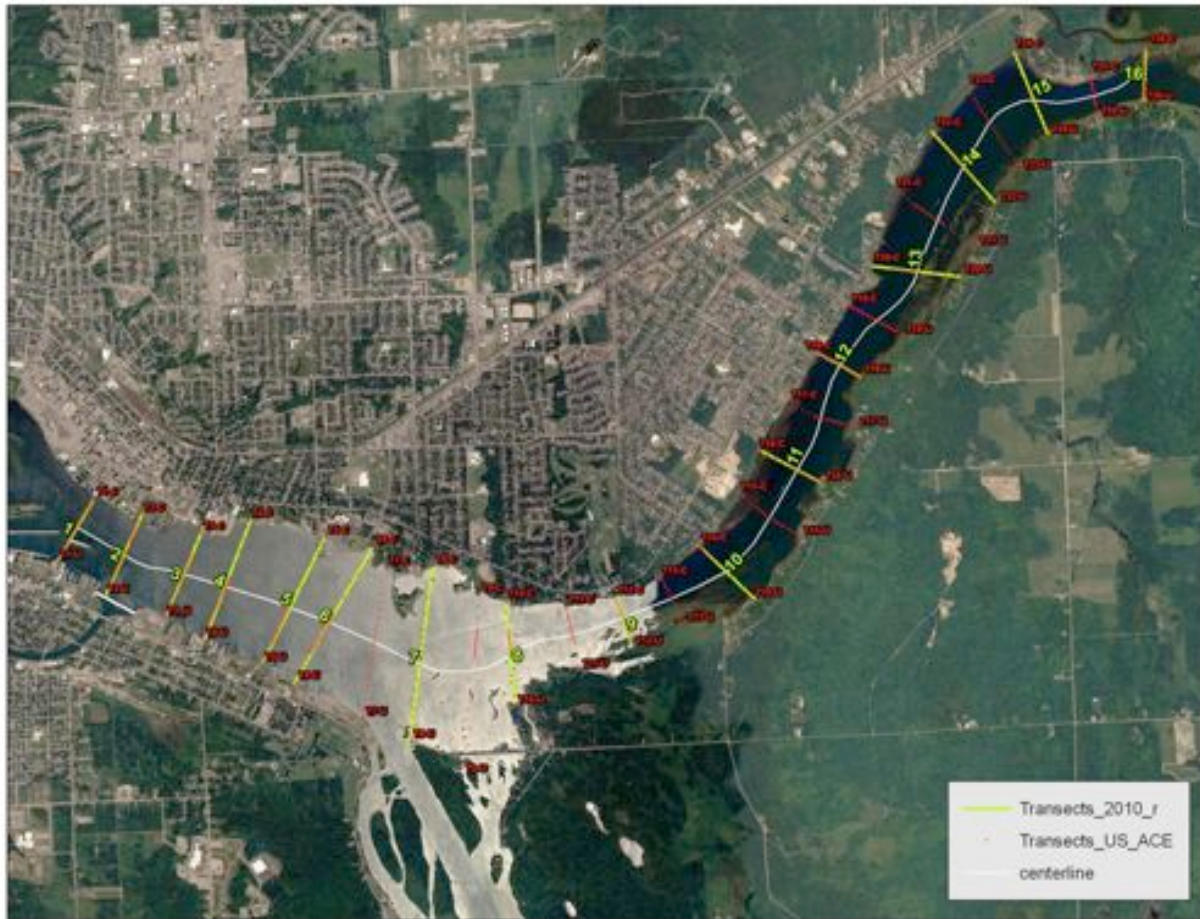


Fig. 30. Locations of transects where the video imaging was carried out (yellow lines).

Video imaging carried out in the river reach shows that the bed of the river is very heterogeneous. Near the banks, the river bed consists of fine sediment deposits with a substantial portion of the bed covered with vegetation. The vegetation traps fine sediment and promotes the deposition. Plants also provide erosion stability for the deposited sediment. In the central part of the river, especially in the navigational part of the river (between transects 1 to 7), the bed is covered with large stones with sharp edges (similar to the ones used in engineering works) and also some rounded cobbles. Evidence of patches of sand can also be observed in this part of the river bed. Downstream of transect 9, the central part of the river is covered with sand and occasional cobbles and pebbles.

The video images captured during the field survey in all transects are stored as digital files in mpeg format. Some of the pictures grabbed from these digital files are shown in Figs. 31 to 34 as examples of typical pictures of the river bed.

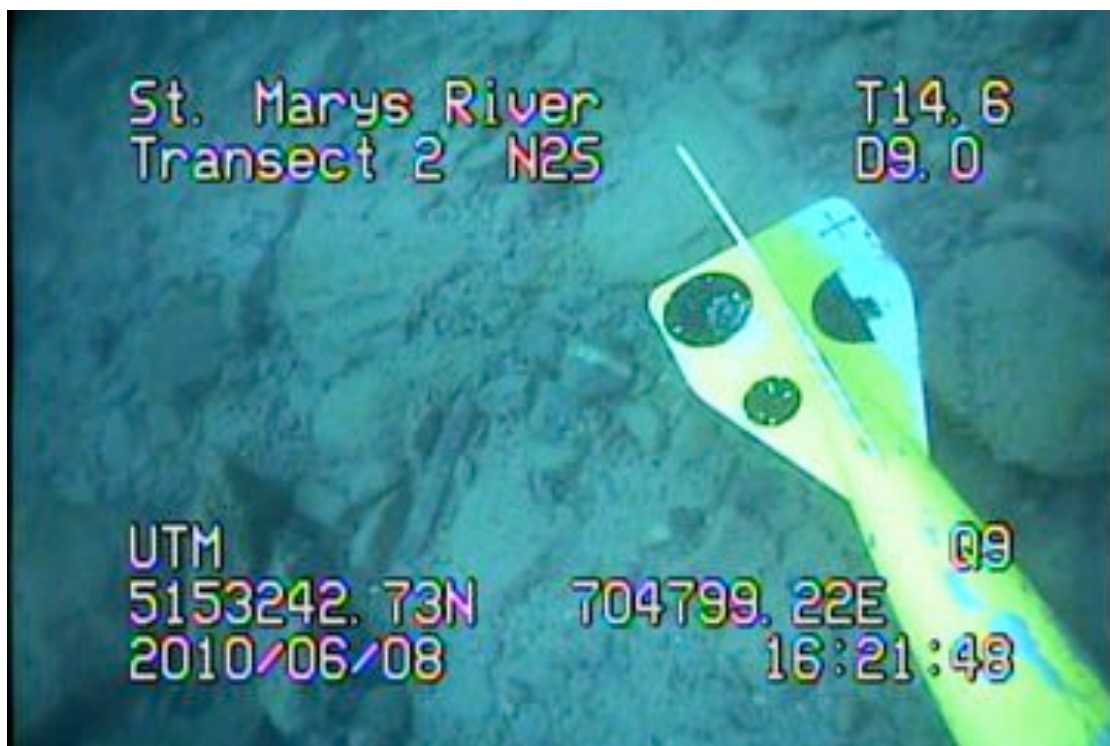


Fig. 31. An image grabbed from a video clip of Transect 2.

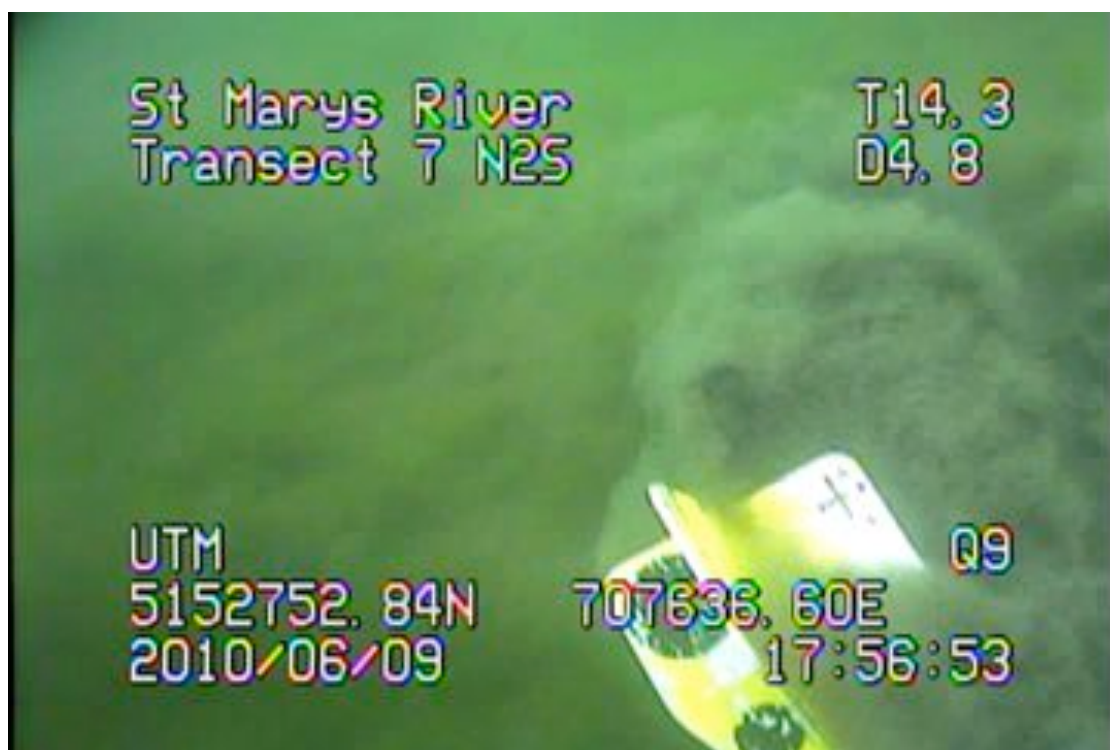


Fig. 32. An image grabbed from a video clip of Transect 7.



Fig. 33. Grabbed image from video clip of Transect 7 showing the vegetation and the fine sediment cloud created when the fish weight hit the river bed.



Fig. 34. Grabbed image from the video clip of Transect 9 showing the presence of angular rocks.

8.2 Grab sampling of the river bed sediment:

In addition to video imaging, grab sampling of the river bed sediment was carried out at a number locations along the transects shown in Fig. 30 to determine the size distribution of the bed sediment. A Shipek sampler was used for this purpose. The Shipek sampler is known to work well for collecting fine grained bottom sediment and hence its use was confined to locations where the sediment is fine. No attempt was made to collect samples in the central part of the river where the bed consisted of angular stones and rounded cobbles. Table 1 shows the sample id, sample location in UTM coordinates and the bed shear stresses predicted by the model for three different flow conditions at the sampling sites.

Table 1. Sample identification and location of grab samples.

Sample id	Location of sampling sites		Bed shear stress in Pa		
	Northing	Easting	Low flow	Mean flow	High flow
SMR-T1-1	5153289.15	704252.1	0.198	0.235	1.106
SMR-T2-1	5153370.34	704856.63	0.242	0.347	1.533
SMR-T2-2	5153158.94	704761.7	0.211	0.26	1.203
SMR-T2-3	5152982.11	704685.97	0.194	0.194	0.949
SMR-T3-1	5153293.99	705451.34	0.107	0.347	1.164
SMR-T3-2	5153138.15	705382.62	0.162	0.373	1.447
SMR-T3-3	5152981	705317.68	0.228	0.463	1.808
SMR-T4-1	5153209.47	705835.33	0.078	0.247	0.838
SMR-T4-2	5152717.24	705645.57	0.202	0.457	1.662
SMR-T4-3	5152505.5	705562.03	0.124	0.05	0.476
SMR-T7-1	5152281.46	707562.85	0.28	0.459	1.823
SMR-T9-1	5152776.83	709356.55	0.384	0.594	2.6
SMR-T9-2	5152725.68	709384.73	0.391	0.665	2.728
SMR-T10-1	5153219.22	710198.89	0.231	0.367	1.563
SMR-T10-2	5153149.77	710270.35	0.214	0.372	1.505
SMR-T10-3	5153053.64	710368.88	0.142	0.233	0.986
SMR-T10-4	5152915.06	710511.72	0.029	0.031	0.155
SMR-T11-1	5154083.21	710855.37	0.022	0.02	0.143
SMR-T11-2	5154025.22	710975.1	0.06	0.124	0.506
SMR-T11-3	5153974.19	711070.07	0.086	0.164	0.669
SMR T12-1	5154981.07	711395.45	0.068	0.115	0.464

SMR-T12-2	5154947.82	711444.52	0.075	0.147	0.56
SMR-T12-3	5154899.38	711539.92	0.074	0.142	0.63
SMR-T13-1	5155874.59	711845.06	0.058	0.097	0.42
SMR-T13-2	5155860.62	711955.94	0.11	0.184	0.779
SMR-T13-3	5155839.05	712075.69	0.114	0.187	0.761
SMR-T14-1	5157038.2	712365.76	0.023	0.02	0.125
SMR-T14-2	5156878.31	712493.55	0.046	0.083	0.348
SMR-T14-3	5156760.38	712602.29	0.073	0.15	0.556

The grab samples collected were photographed and analyzed for size distribution in the laboratory. Some typical photographs of the samples are shown in Figs. 35 to 37. Photographs of all the samples are shown in Appendix-B.

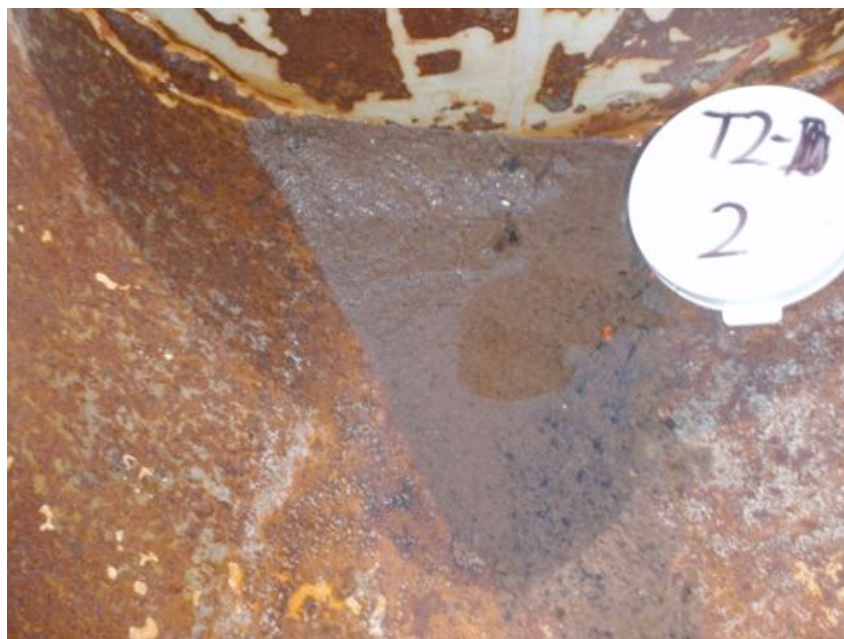


Fig. 35. A photograph of grab sample collected at Transect No. 2 (Sample id: SMR-T2-2)



Fig. 36. A photograph of grab sample collected at Transect 3 (Sample id: SMR-T3-1)

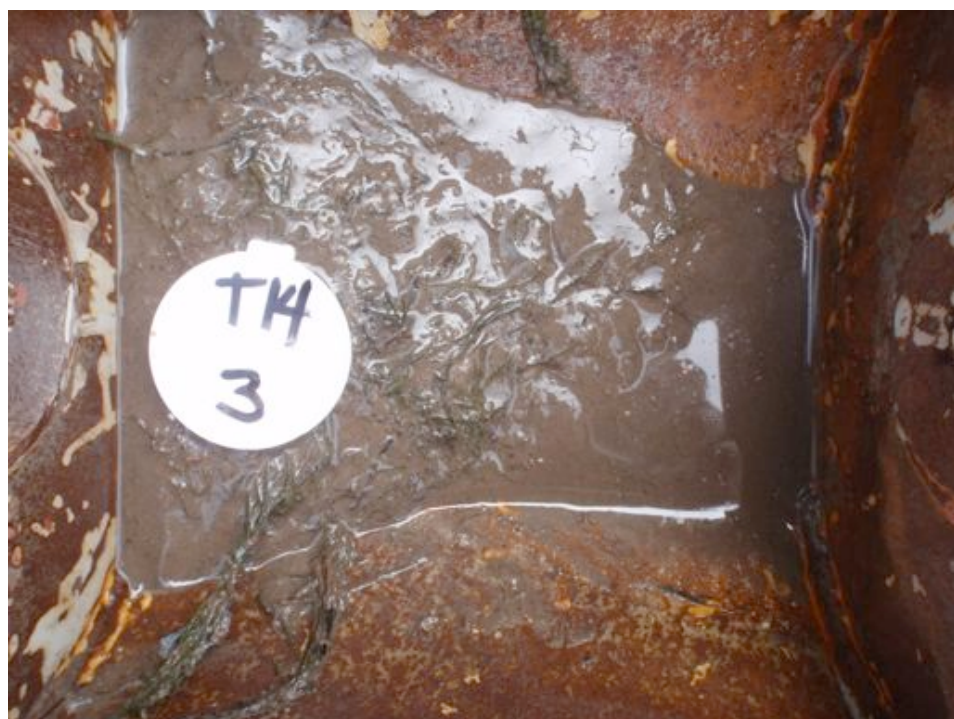


Fig. 37. A photograph of grab sample collected at Transect 14 (Sample id: SMR-T14-3).

The grab samples collected were analyzed for size distribution in the Sedimentological Laboratory of Environment Canada's National Water Research Institute in Burlington, Ontario. A typical result from the size analysis is shown below:

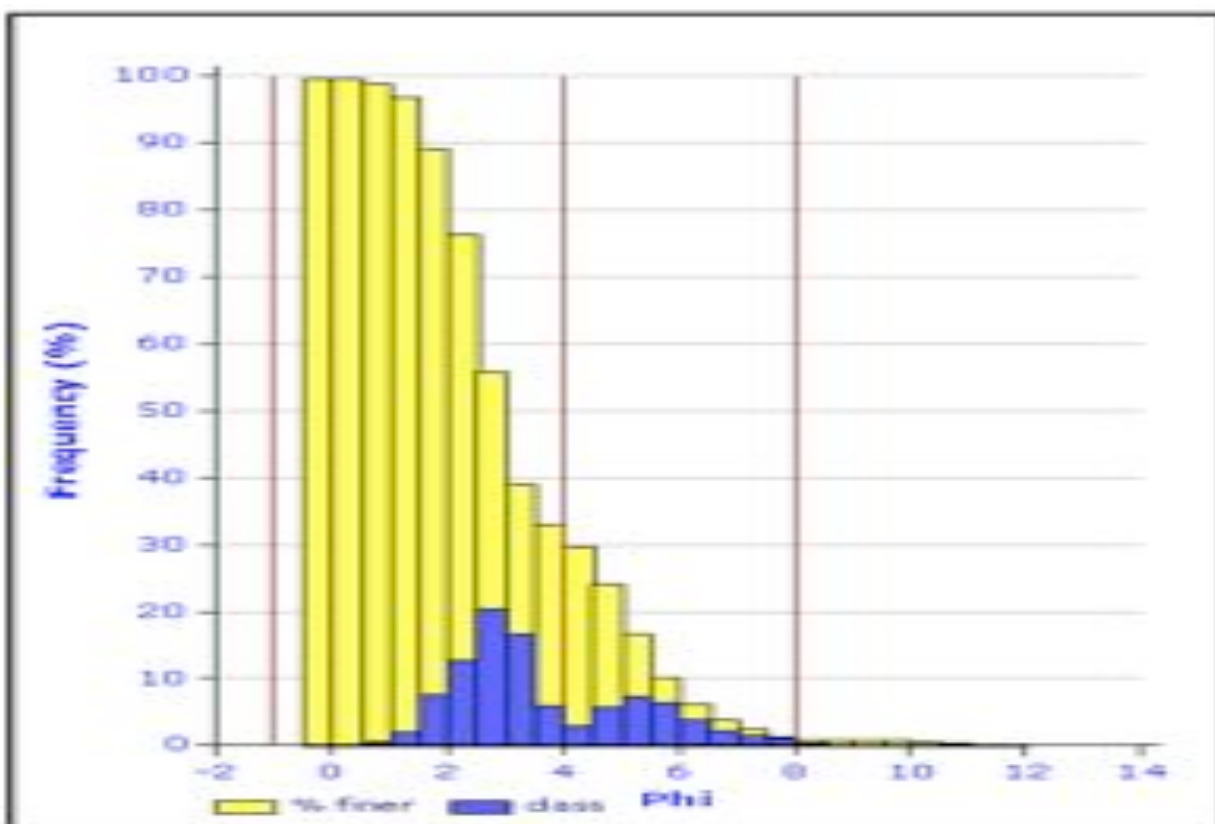
NWRI SEDIMENTOLOGY LABORATORY

Particle Size Analysis Results (v. 2.23)

RUN INFORMATION

Run No	3006	<i>SMR-T12-2</i>
Batch No	197	<i>ST. MARYS RIVER</i>
Client ID	BIBERHOFER	<i>HANS BIBERHOFER</i>
Sample Wt (g)	5.8447	
Instruments	Sieve + Horiba	
Submitted	01-Dec-10	
Last Updated	05/01/2011 10:19	
Exported	05/01/2011 10:19	

Micron Interval	Freq (%)	% Finer	Micron Interval	Freq (%)	% Finer
1000-1414.21	0.188	99.81	3.91-5.52	1.097	1.365
707.11-1000	0.209	99.6	2.76-3.91	0.464	0.901
500-707.11	0.683	98.92	1.95-2.76	0.089	0.812
353.55-500	2.009	96.91	1.38-1.95	0	0.812
250-353.55	7.684	89.23	0.98-1.38	0	0.812
176.78-250	12.86	76.37	0.69-0.98	0.119	0.693
125-176.78	20.55	55.82	0.49-0.69	0.362	0.33
88.39-125	16.77	39.05	0.35-0.49	0.284	0.046
62.5-88.39	6.033	33.02	0.24-0.35	0.046	0
44.19-62.5	3.113	29.9			
31.25-44.19	5.793	24.11	Total %	100	
22.1-31.25	7.348	16.76			
15.63-22.1	6.503	10.26			
11.05-15.63	3.93	6.33			
7.81-11.05	2.296	4.034			
5.52-7.81	1.572	2.462			



COMPOSITION & CLASSIFICATION

% Gravel	0	PERCENTILES		
% Sand	66.984	%	Phi	Microns
% Silt	31.652	5	1.624	324.3
% Clay	1.365	16	2.203	217.1
% Gravel+Sand	66.984	25	2.533	172.7
% Silt+Clay (= Mud)	33.016	35	2.777	145.9
Silt/Mud	0.959	50	3.173	110.8
(Gravel+Sand)/Mud	2.029	75	4.923	32.96
Sand/Mud	2.029	84	5.559	21.22
Silt/Clay	23.195	95	6.79	9.04

Fig. 38. An example of the results from the size analysis of the grab samples.

A summary of the size distribution data for all samples are listed in Table 2.

Table 2. Summary of the size distribution data for all grab samples.

Sample id	% Gravel	%sand	%silt	D50 in μm	Folk Label-GMS
SMR-T1-1	0.00	97.58	2.42	183.10	SAND
SMR-T2-1	0.00	99.72	0.28	256.30	SAND
SMR-T2-2	0.26	99.22	0.52	325.70	slightly gravelly SAND
SMR-T2-3	0.00	99.45	0.55	219.70	SAND
SMR-T3-1	0.00	99.60	0.40	279.30	SAND
SMR-T3-2	2.16	97.44	0.40	372.90	slightly gravelly SAND
SMR-T3-3	1.18	98.71	0.11	335.80	slightly gravelly SAND
SMR-T4-1	0.00	99.37	0.63	209.20	SAND
SMR-T4-2	0.00	99.96	0.04	395.50	SAND
SMR-T4-3	0.00	98.05	1.95	184.10	SAND
SMR-T7-1	48.06	51.07	0.87	1785.00	sandy GRAVEL
SMR-T9-2	46.26	53.50	0.24	1504.00	sandy GRAVEL
SMR-T9-1	93.30	6.68	0.02	6009.00	GRAVEL
SMR-T10-1	29.32	70.34	0.34	368.80	gravelly SAND
SMR-T10-2	0.19	99.36	0.45	240.30	slightly gravelly SAND
SMR-T10-3	0.00	14.37	85.63	24.63	sandy MUD
SMR-T10-4	0.00	15.33	84.67	24.06	sandy MUD
SMR-T11-1	0.00	23.58	76.42	31.40	sandy MUD
SMR-T11-2	0.00	96.82	3.18	164.80	SAND
SMR-T11-3	1.97	97.22	0.82	230.80	slightly gravelly SAND
SMR-T12-1	0.00	97.91	2.09	272.80	SAND
SMR-T12-2	0.00	66.98	33.02	110.80	muddy SAND
SMR-T12-3	N/A	N/A	95.68	23.75	Cannot calc: Sand/Mud = N/A
SMR-T13-1	N/A	N/A	97.42	24.33	Cannot calc: Sand/Mud = N/A
SMR-T13-2	0.14	99.08	0.78	301.30	slightly gravelly SAND
SMR-T13-3	28.47	71.23	0.30	415.50	gravelly SAND
SMR-T14-1	N/A	N/A	97.04	24.81	Cannot calc: Sand/Mud = N/A
SMR-T14-2	0.10	95.88	4.03	158.70	slightly gravelly SAND
SMR-T14-3	0.00	63.43	36.57	98.84	muddy SAND

From Table 2, we can see that a majority of the samples collected are classified as slightly gravelly sand, gravelly sand and sand (a total of 18 samples). There are some coarse samples classified as sandy gravel and gravel (a total of three) and some fine sediment samples classified as sandy mud, muddy sand and

unclassified (a total of eight samples). For the sandy mud and unclassified samples (six in number), the median size of the sediment is below 62 microns, which is considered as a distinguishing-size that separates the cohesive sediment from the non-cohesive counterpart. In other words, if the median size of the sediment is less than 62 microns, then the sediment is considered as cohesive sediment; otherwise, it is considered as non-cohesive.

The behaviour of the cohesive sediment is very different from that of the non-cohesive sediment. The main difference lies in the fact that the cohesive sediment tends to flocculate and form agglomeration of particles when subjected to a flow field, whereas the non-cohesive sediment behaves as individual particles. Our knowledge of the transport characteristics of the non-cohesive sediment is far more advanced than our knowledge for the cohesive sediment. For example, the determination of the critical shear stress for erosion of the non-cohesive sediment is possible from the existing theories, whereas the same for the cohesive sediment has to be obtained from field experiments.

8.3 Computation of critical shear stress for erosion for non-cohesive sediment:

Knowing the size characteristics of bed sediment, it is possible to calculate the critical shear stress for erosion of the non-cohesive sediment from existing theories. For example, Shields' diagram is often used to calculate the critical shear stress for non-cohesive sediment. In this work, a modified Shields' diagram as given by Yalin and Karahan (1979) was used to calculate the critical shear stress for grab samples whose median size was greater than 62 microns. The Shields' diagram presented by Yalin and Karahan (1979) requires a trial and error solution and is not very convenient for computations using digital computers. To overcome this difficulty, DaSilva and Bolisetta (2000) developed an approximate analytical expression for the Shields' diagram. The analytical expression of DaSilva and Bolisetta (2000) is used here. The expression is as follows:

$$\tau_* = 0.13 d_*^{-0.392} \exp(-0.015 d_*^2) + 0.045(1 - \exp(-0.068 d_*)) \quad (7)$$

where τ_* and d_* stand for

$$\tau_* = \frac{\tau}{(\gamma_s - \gamma)d} \quad (8)$$

and

$$d_* = d \left[\frac{(\gamma_s - \gamma)g}{\nu^2} \right]^{\frac{1}{3}} \quad (9)$$

In the above expressions, τ is the critical shear stress for erosion, γ_s is the specific weight of sediment, γ is the specific weight of water, d is the median size of sediment, g is acceleration due to gravity and ν is the kinematic viscosity of water. Assuming the specific weight of sediment to be 2650 Kg/m³, the critical shear stress values were computed for samples that have particles larger than 62 microns and are summarized in Table 3.

Table 3: Computation of critical shear stress for erosion of grab samples that are non-cohesive.

Sample id	D50 in μm	d-star	τ -star	τ -critical in Pa
SMR-T1-1	183.10	4.62739185	0.0638662	0.19
SMR-T2-1	256.30	6.47733769	0.04934036	0.20
SMR-T2-2	325.70	8.23124809	0.0398809	0.21
SMR-T2-3	219.70	5.55236477	0.05596074	0.20
SMR-T3-1	279.30	7.05860482	0.04577448	0.21
SMR-T3-2	372.90	9.42410934	0.03553046	0.21
SMR-T3-3	335.80	8.48650018	0.03881668	0.21
SMR-T4-1	209.20	5.28700368	0.05808851	0.20
SMR-T4-2	395.50	9.99526748	0.03397635	0.22
SMR-T4-3	184.10	4.65266433	0.06363107	0.19
SMR-T7-1	1785.00	45.1113842	0.04290597	1.24
SMR-T9-2	1504.00	38.0098162	0.04160605	1.01
SMR-T9-2	6009.00	151.862357	0.04499853	4.38
SMR-T10-1	368.80	9.32049216	0.03584743	0.21
SMR-T10-2	240.30	6.07297794	0.05208713	0.20
SMR-T10-3	24.63	0.62246128	0.15750714	N/A
SMR-T10-4	24.06	0.60805597	0.15894178	N/A
SMR-T11-1	31.40	0.793556	0.14335987	N/A
SMR-T11-2	164.80	4.16490539	0.06838587	0.18
SMR-T11-3	230.80	5.83288934	0.05382522	0.20
SMR-T12-1	272.80	6.89433368	0.04673748	0.21
SMR-T12-2	110.80	2.80019124	0.08499305	0.15
SMR-T12-3	23.75	0.6002215	0.15974194	N/A
SMR-T13-1	24.33	0.61487954	0.15825641	N/A
SMR-T13-2	301.30	7.61459948	0.0427695	0.21
SMR-T13-3	415.50	10.5007172	0.03285806	0.22
SMR-T14-1	24.81	0.62701033	0.15706362	N/A
SMR-T14-2	158.70	4.01074323	0.06999153	0.18
SMR-T14-3	98.84	2.49793233	0.08971802	0.14

An assessment of the stability of the non-cohesive sediment samples can be made by comparing the critical shear stress values with the bed shear stress values that are likely to be prevailing at sampling sites for different flow conditions (low, mean and high flows). Such a comparison is made in Fig. 39.

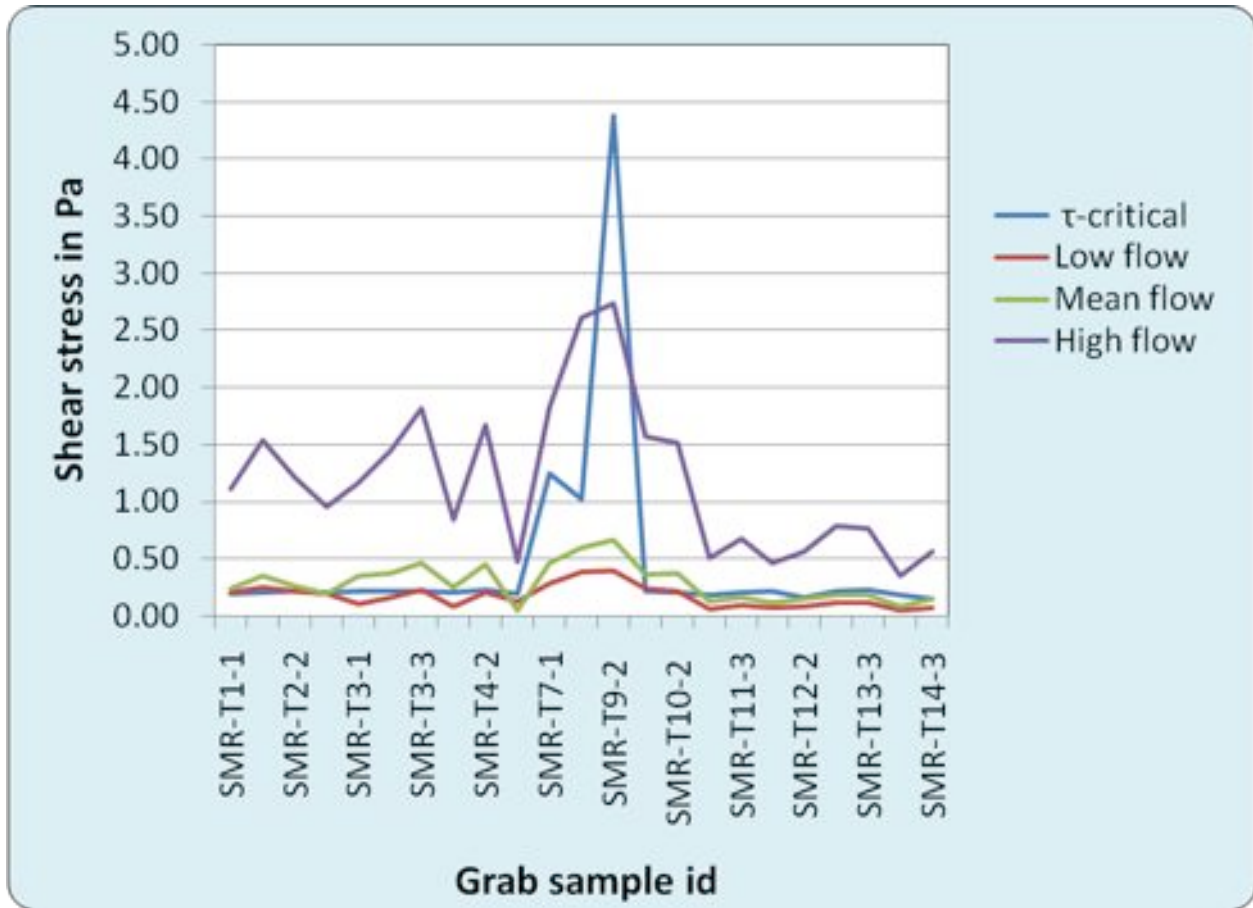


Fig. 39. Comparison of bed shear stresses with critical shear stresses for erosion of non-cohesive grab samples.

From Fig. 39, we can see that the critical shear stress values for the grab samples are slightly higher than the low flow shear stresses. Therefore, the sediment will be stable under low flow conditions. But, when the flow rate increases to average or to high flow values, the bed shear stresses exceed the critical shear stress values except for one sample (SMR-T9-2). Therefore, under these flows, the majority of the non-cohesive sediment at the sampling locations will be mobile and will be transported to areas where the shear stresses are lower. Therefore, the non-cohesive sediment regime in the St. Marys River can be considered to be highly dynamic. It should be noted that non-cohesive sediment are usually clean and do not contribute to the transportation of contaminants through the river system.

It should be reiterated here that the methodology used to calculate the critical shear stresses listed in Table 3 is not valid for cohesive sediment, i.e., for samples such as SMR-T10-3, SMR-T10-4, SMR-T11-1, SMR-T12-3, SMR-T13-1, SMR-T14-1, whose median size is less than 62 microns. For such cohesive sediment, a field methodology employing an in-situ erosion flume was used and the critical shear

stresses for erosion were measured directly. The details of the in-situ erosion flume and the measurement methodology are given in the following section.

8.4 Measurement of critical shear stress for erosion of cohesive sediment:

The in-situ erosion flume used in the present study consists of a rectangular duct, which is 3.5 m in length, 0.30 m in width and 0.06 m in depth. The bottom part of the flume is open over a length of 1.0 m and a width of 0.30 m (test section- made out of plexiglass) and it begins at a distance of 1.75 m from the flume entrance. The entrance section of the flume consists of two segments. The first segment is a smoothly contracting section that accelerates the flow as it enters the flume. The second section is a flow establishment section and contains a set of straight acrylic tubes over the whole cross section to damp out any secondary circulation. Downstream of the test section, the flume contracts gradually into a circular cross section and connects to a pump that draws water through the flume and discharges to the ambient. The flow rate of the pump is controlled electronically and a digital read-out provides a measure of the flow rate. When the flume is resting on the sediment bed properly, the surface of the bed will be in line with the bottom plate of the flume on both end-sections of the flume. A photograph of the flume is shown in Fig.40.



Fig. 40. A photograph of the in-situ erosion flume.

8.4.1 Instrumentation:

The flume is equipped with a Pitot tube to measure the flow velocity at a fixed point in the flow field, and an optical instrument to measure the concentration of the eroded sediment. The optical

instrument, known as OSLIM was manufactured by the Delft Hydraulics Laboratory in The Netherlands. It consists of an infrared light emitting diode and a photodiode mounted on either side of a glass tube through which a sample containing the eroded sediment is pumped. The relationship between the photodiode output in Volts and the concentration of the sediment is obtained by calibration. In addition, an OBS probe, which operates on the principle of back scattering of light was installed on the flume as a backup probe for measuring the concentration of the eroded sediment. The flume is fitted with two under-water video cameras, one looking from the top and the other from the side. The camera mounted at the top is used during flume deployment and the side looking camera is used to observe the erosion of the bed.

8.4.2 Calibration:

The relationship between the flow rate through the cross section and the bed shear stress induced by the flow on the exposed bed surface is obtained in a calibration experiment in the laboratory. For measuring the bed shear stress, the Pitot tube was used as the Preston tube by positioning the tube against a “false” flume bed made up of smooth plywood. By measuring the difference between the static and dynamic pressures at this position, the bed shear stress can be calculated using the calibration equation that was established by Patel for Preston tube assemblies. The measured relationship between the bed shear stress and the flow rate is shown in Fig. 41.

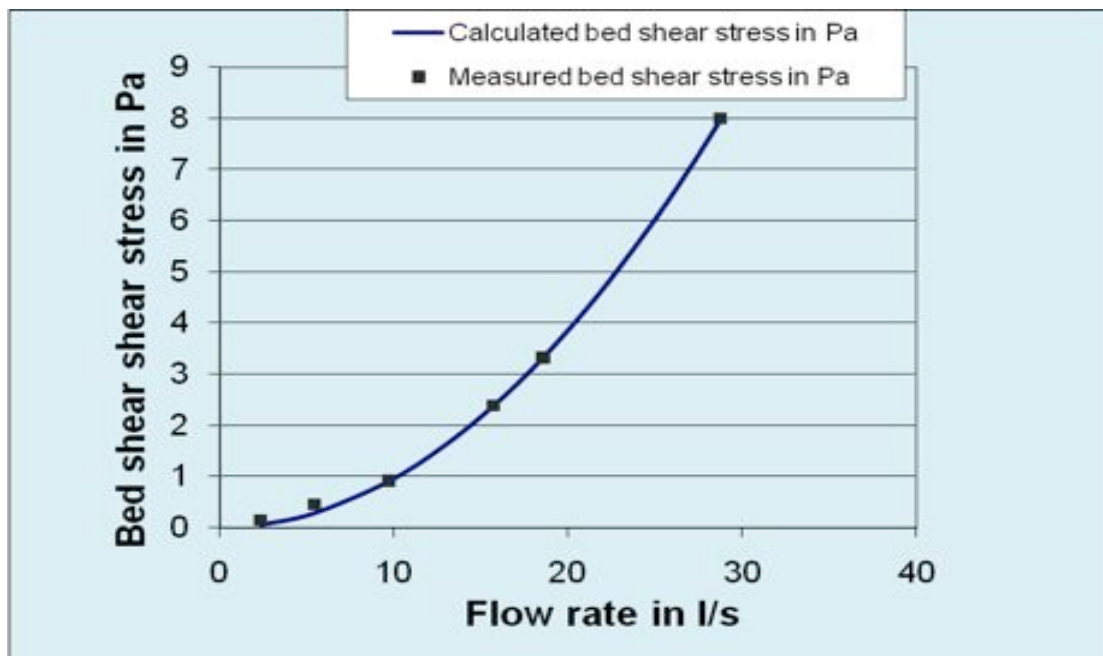


Fig.41. Relationship between the flow rate and the bed shear stress

Also shown in this figure is a regression equation, which has the form similar to that of the Darcy-Weisbach friction factor equation. The form of the equation is as follows:

$$\tau = 0.0096Q^2 \quad (10)$$

where τ is the bed shear stress in N/m^2 and Q is the flow rate in L/s . The above regression equation shows close agreement with the measured relation as can be seen in Fig.41, and hence it is adopted for estimating the bed shear stress in the in-situ erosion flume.

The flow rate, Q of the pump is controlled electronically and a digital display provides a read-out that is proportional to Q . Actual relationship between the display read-out and the flow rate was obtained by laboratory measurement using a laboratory tank. The flume was operated at different flow rate settings ("flow degrees") and for each setting, the flow rate was measured by collecting the discharge from the pump into a pre-weighed tank for a known period of time. The plot showing the "flow degrees" versus the flow rate in L/s is shown in Fig. 42.

For each "flow degree" setting, the Pitot tube voltage was also measured, which is another measure of the flow rate. But, for establishing the flow rate during the operation of the flume in the field, the calibration shown in Fig. 42 was used. The bed shear stress was then computed using equation 10.

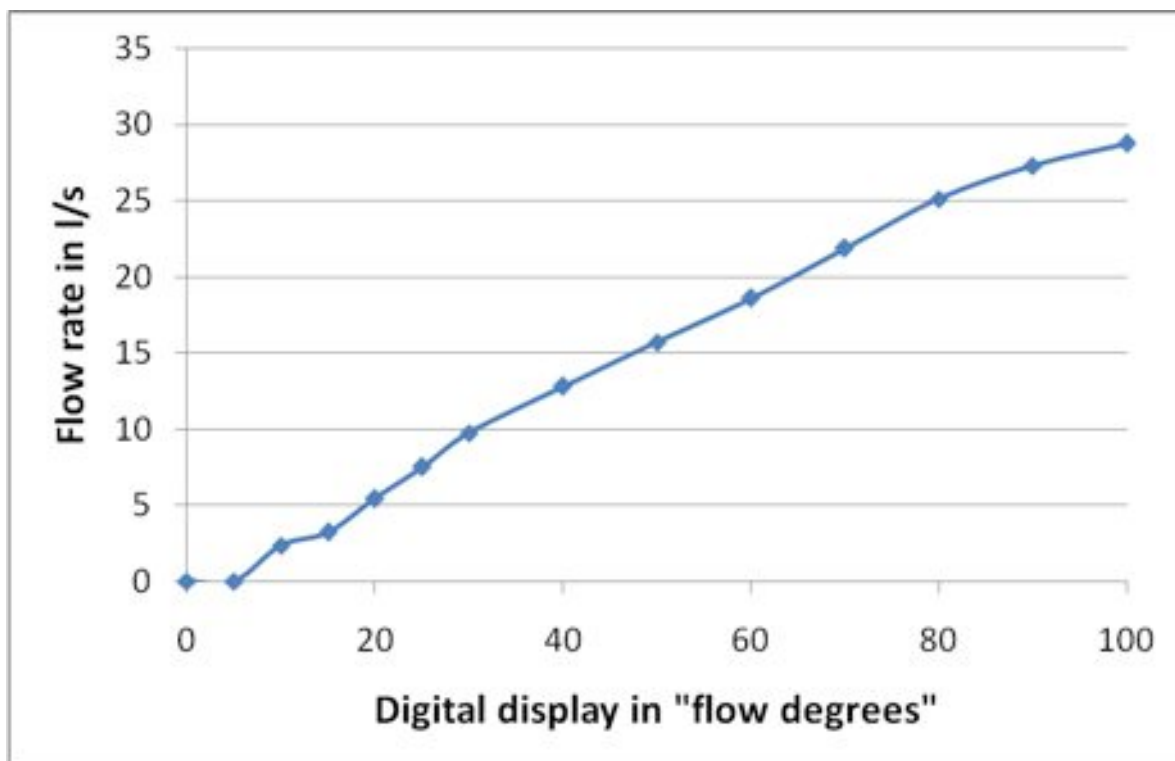


Fig. 42. Relationship between the flow rate and the read-out in "flow degrees".

8.4.3 Operation of the flume in the field:

The flume was deployed from a pontoon floating platform (see the photograph in Fig. 43).



Fig.43. Deployment of the in-situ erosion flume.

The pontoon is tied to a boat and the boat was anchored at the study sites while the flume was lowered into the water. Positioning of the flume on the sediment deposit was aided by the underwater video camera installed in the flume and the divers. Once the flume was in place, the pump was started and the flow rate was increased in steps. Each flow rate step was maintained for a period of time depending on the erodibility of the sediment (usually for about 15 minutes). The sites at which the flume was

deployed are indicated in Fig.44 as white dots. The location of the flume sites and the shear stresses computed by the model for different flow conditions at these sites are summarized in Table 4.



Fig. 44. Locations of the in-situ erosion flume measurement sites (shown as white dots).

Table 4. Locations of flume sites and the shear stresses predicted by the model for these sites.

Flume site id	Location of flume sites		Bed shear stress in Pa		
	Northing	Easting	Low flow	Mean flow	High flow

10SSM_ISF32	5153419	705884	0.025	0.034	0.22
10SSM_ISF01	5153418	706079	0.024	0.02	0.14
10SSM_ISF_vortex	5152793	707714	0.001	0.002	0.007
10SSM_ISF09	5152659	708017	0.033	0.03	0.105
10SSM_ISF04	5152549	707788	0.055	0.082	0.258

From Table 4, it can be seen that the bed shear stresses under different flow conditions are considerably lower than the shear stresses for the grab sample sites (Table 1). Consequently, the flume sites behave as depositional sites and the sediment deposited are very fine and cohesive. This was confirmed by the flume tests. At all the flume sites tested, the sediment at the top layer was very fluffy and erodible and the very first shear stress step of the flume (flow degree of 10%) eroded all of fluff layer. Because of the initial high concentration of the eroded sediment, the OSLIM failed to work and hence the measure of the concentration of the eroded sediment for different shear stress levels is not available. Fortunately, the under- water video camera mounted on the side of the flume provided the visual images of the sediment erosion process. It also gave a qualitative estimation of depth of erosion of the sediment for various shear stress levels. From these video images, it was observed that the erosive resistance of the sediment increased as the function of the depth of sediment. This is a characteristic property of a cohesive sediment deposit. In such deposits, the density of the deposit would increase as a function of depth due to self weight consolidation process.

From the flume tests, it was estimated that the critical shear stress for the top five centimetre of the fluff sediment is about 0.05 Pa (first shear stress step of the in-situ erosion flume), and the depth of erosion will be limited to about 5 cm for the maximum shear stress that can be encountered in these sites (0.26Pa).

From the results of video imaging work, grab sample analysis and the in-situ erosion flume experiments, we can draw some general conclusions regarding the sediment transport regime in the St. Marys River and some specific conclusions regarding the stability of the sediment under different flow conditions. In the central part of the river, especially in the navigational part, the bed of the river consists of large angular stones, rounded cobbles and pebbles. These materials possess very high critical shear stress values and hence can withstand the erosive power of the high flow. Therefore, these materials can be considered as stable under all three flow conditions.

In the central part of the river downstream of the navigational channel branch off, the river bed consists of sand and fine gravel, which possess moderate critical shear stress values and they are stable only at the low flow condition. At average and high flows, the material can be mobilized by the flow and can be transported to regions of lower shear stresses. Therefore, these materials can be considered to have partial stability under specific flow conditions. These materials are usually non-cohesive and considered clean. Contaminant transport associated with these materials is usually negligible.

In the flow circulation zones and in regions near the banks of the river where the bed shear stresses are very low, the bed consists of very fine and cohesive sediment. These areas are in general depositional areas, and deposition of fine sediment occurs under almost all flow conditions. The fine sediment deposits exhibit a strong vertical gradient in the erosive resistance: At the top layer, the material is very fluffy and is easily erodible. As the depth of erosion increases, the erosion resistance of the deposit increases. The critical shear stress for the top layer was estimated to be at 0.05 Pa. At the depth of erosion of 5cm, the erosive resistance can be as high as 0.29 Pa. The fine sediment deposits below 5cm depth can be considered to be stable under all three flow conditions. Fine sediments have high affinity for contaminants and hence these fine sediment deposits can have high concentration of contaminants.

9.0 Impacts of water level changes

When simulating flow characteristics using the RMA2 model, the water levels at the downstream boundary of the modelling domain are used as the boundary condition for the model. Therefore, changes in the water levels are taken into account in the simulation of St. Marys River flows using the RMA2 model. As mentioned earlier, for the present modelling study, the coarse grid RMA2 model of USACE was used to provide water levels at the downstream boundary for the present fine grid model. Measured water levels at Thessalon, Slab Dock and Rock Cut channel gauging stations were used as the downstream boundary condition for the coarse grid RMA2 model, thereby accounting the impact of changing water levels in the model simulations.

10.0 Impacts of Ice Cover on Sediment stability

Ice conditions on the St. Marys River can alter the flow velocities and shear stresses and hence can have an impact on sediment stability. Ice conditions in the river are being monitored by different agencies mainly for aiding navigation through the Great Lakes system. Some of the agencies involved in ice monitoring in this part of the Great Lakes include US Army Corps of Engineers (NCE), Great Lakes Environmental Research Laboratory (GLERL), NOAA and US Coast Guard (USCG). Ice data on winter-early spring ice conditions and thicknesses on the St. Marys River are useful to the Corps of Engineers in Detroit District for making decisions regarding re-opening of the Locks at Sault Ste Marie for spring navigation and to evaluate the environmental impacts of navigation with ice-cover. In an unpublished contract report to Detroit District's Corps of Engineers, Lawrence Gatto (1991) analyzed the ice data and mapped the distribution of ice, and estimated the ice thicknesses from 1967 to 1991. He used both aerial photographs and Landsat images to observe the ice distribution in the river.

The effect of the ice covers on flow fields were studied extensively in the literature. For example, Lau and Krishnappan (1985) studied the impact of ice cover on sediment transport using a laboratory channel. Krishnappan (1983) proposed a methodology to predict the suspended sediment profiles in ice covered flows. In another study, Krishnappan (1984) proposed a turbulence model to calculate the flow

conditions in channels with ice cover. The results of these studies have shown that the presence of ice cover can have significant impacts on flow field and sediment transport characteristics. For example, presence of ice cover can cause an increase in flow depth due to the additional roughness presented to the flow by the ice cover. The increases can be of the order of 10 to 25%. In addition, the velocity distribution is drastically modified, and the turbulence level reduced. Consequently, the sediment transport capacity of the ice covered flow is drastically reduced (of the order of 300%). In the study of Lau and Krishnappan (1985), it was found that the bed shear stress in ice covered flows can be calculated knowing the bed shear stress of the free surface flow if the ice-covered flow can be considered in two layers. The layers are separated by the plane of maximum velocity. Considering the lower layer of the ice covered flow as a free surface flow, the bed shear stress for that layer can be calculated as:

$$\tau = \rho g S h_b \quad (11)$$

where h_b is the thickness of the lower layer and S is the slope of the water surface. Using this result and assuming that the increase in flow depth due to the presence of ice cover is approximately equal to 15%, and the thickness of the lower layer is 50% of the flow depth, which is valid for flows with ice-cover roughness equal to bed roughness, the bed shear stress in ice covered flows can be expressed in terms of the shear stress of the free surface flow as follows:

$$\tau_{ice-cover} = 0.575 \tau_{free-surface} \quad (12)$$

Using the above result, bed shear stress distributions for ice covered flows were calculated from the solution of the free surface flows. The shear stress distribution computed for the mean flow is shown in Fig. 45.

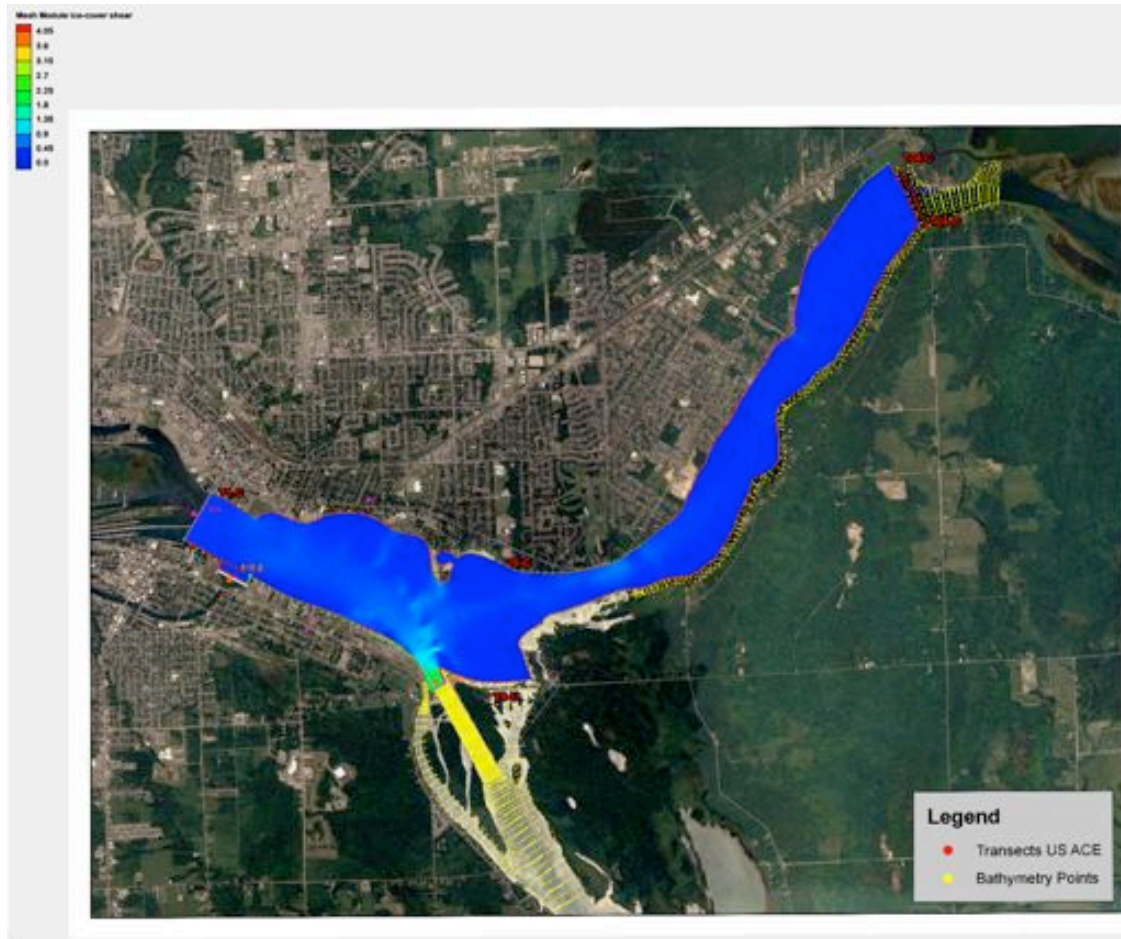


Fig. 45. Shear stress distribution of ice-covered flow under average flow condition.

Similar computations were carried out for low and high flows and the shear stress distributions are obtained. These are depicted in Figs. 46 and 47 respectively.

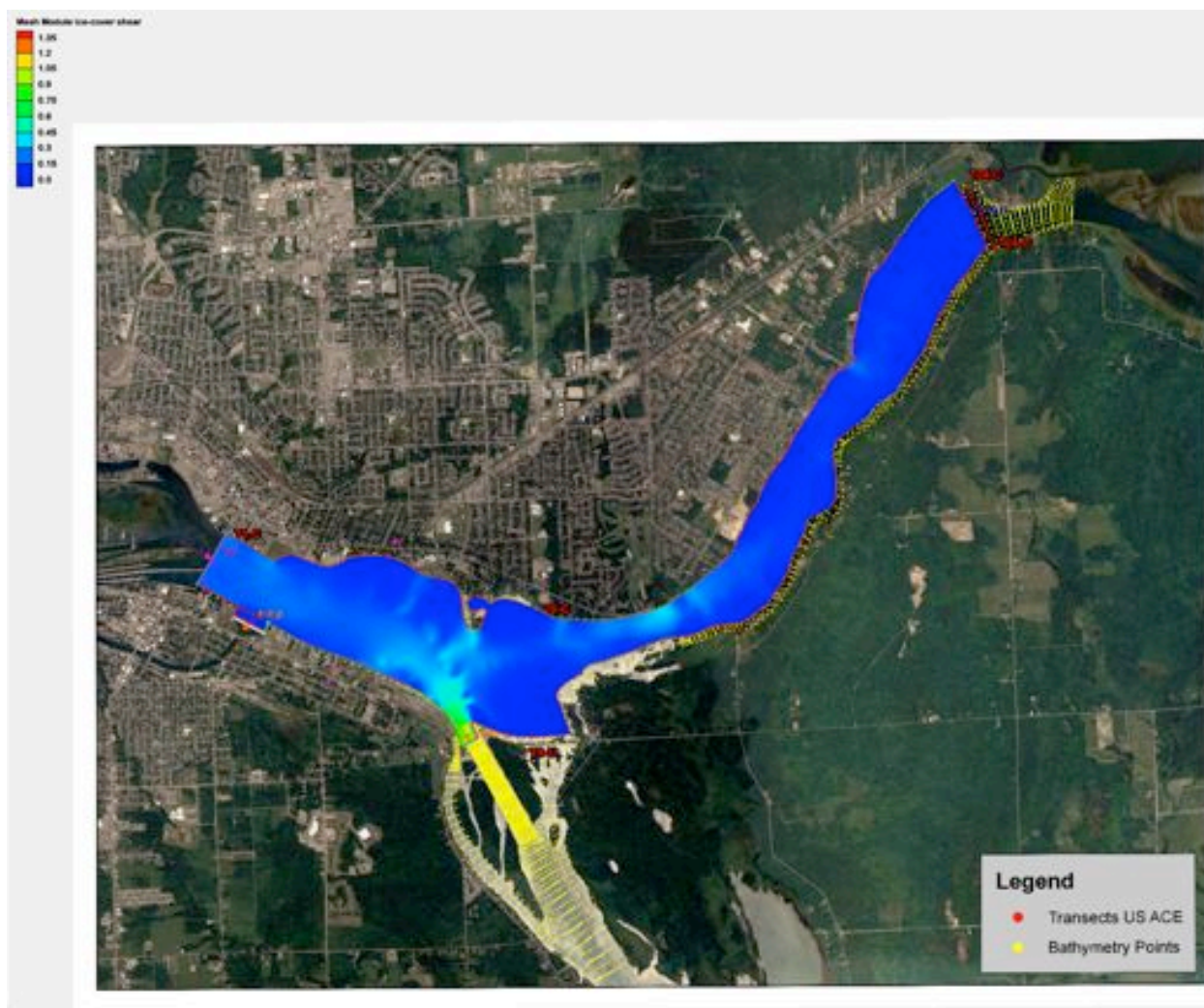


Fig. 46. Shear stress distribution of ice covered flow under low flow condition.

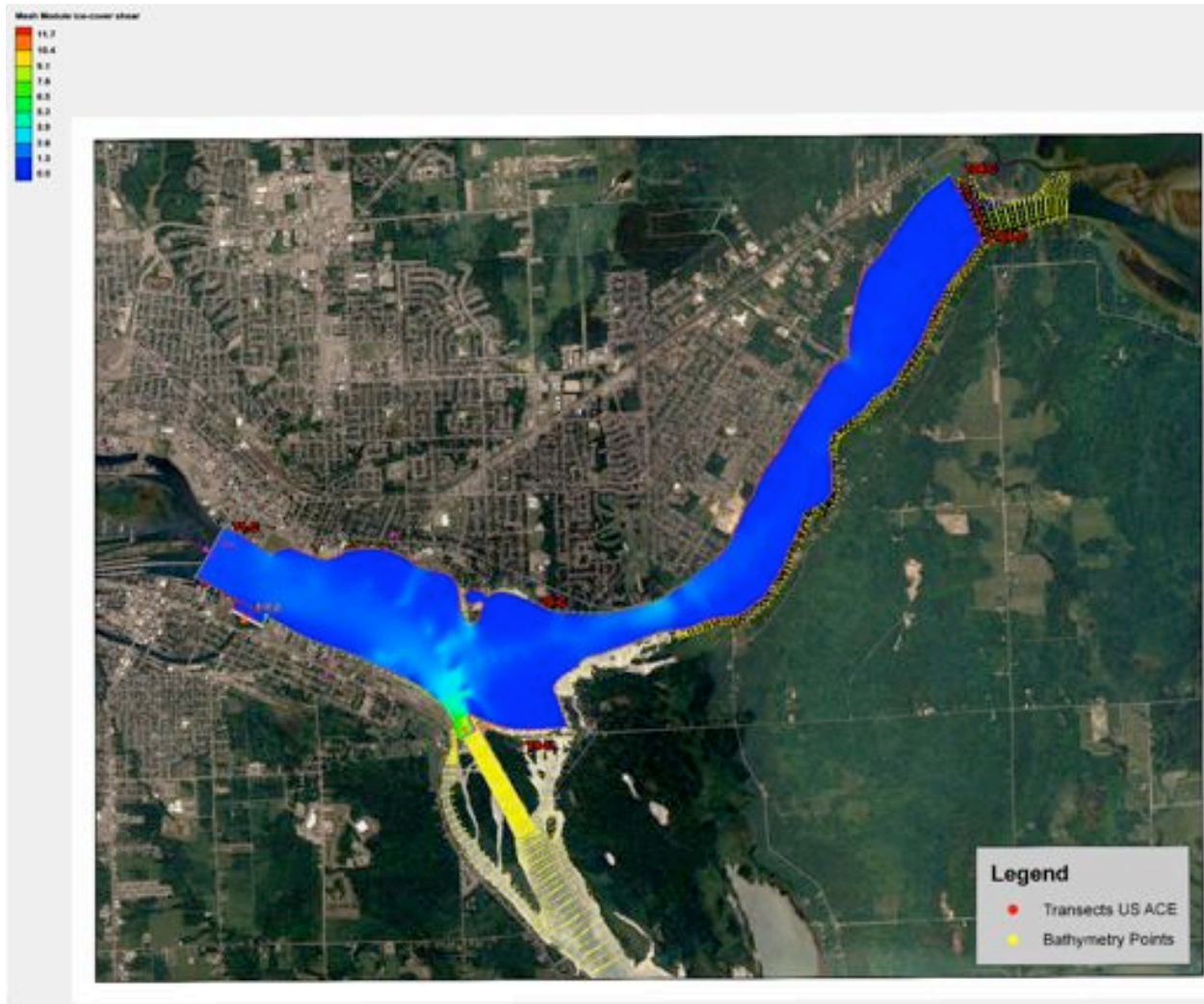


Fig. 47. Shear stress distribution of ice covered flow under high flow condition.

Bed shear stress results for all three ice covered flows are compared along the Transect A as shown in Fig. 48. Comparing this figure with Fig. 28 for free surface flows, we can see that the bed shear stresses are lower for ice covered flows compared to that for the free surface counterparts. Lowering of the bed shear stress in ice covered flows has implications for sediment stability in such flows.

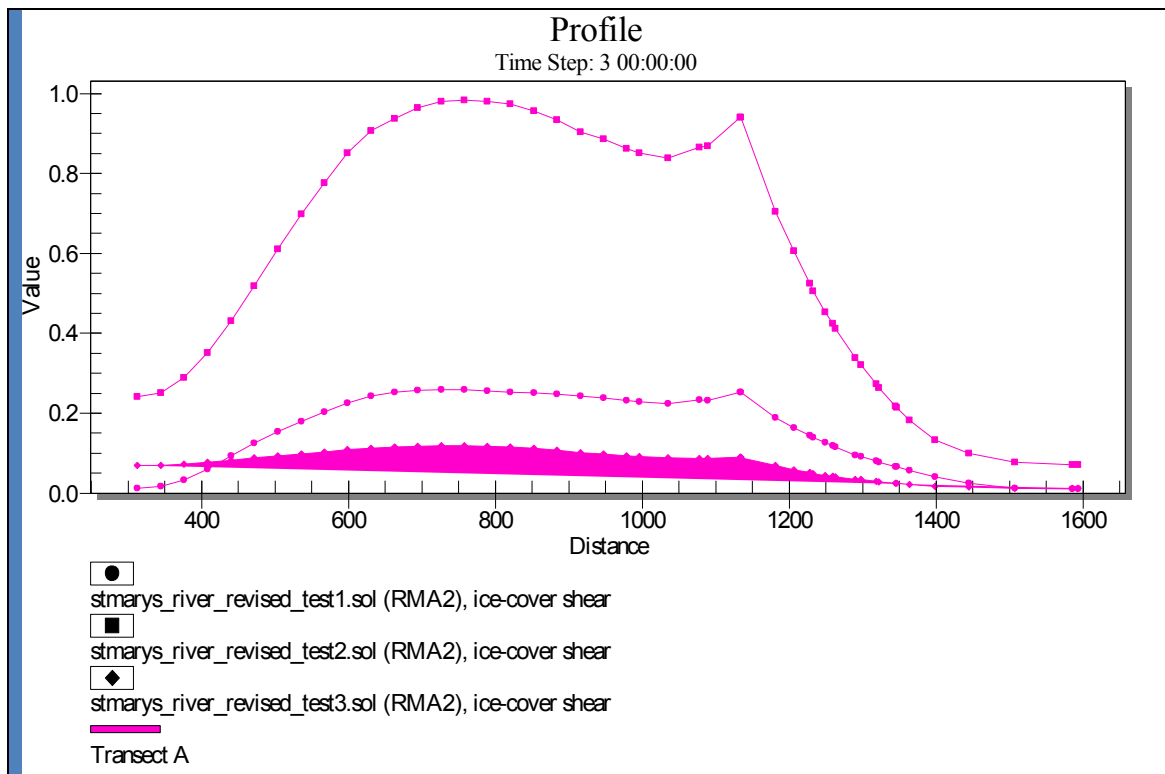


Fig. 48. Shear stress distribution for ice covered flows along the transect A.

To assess the stability of sediment in ice covered flows, the critical shear stress for non-cohesive grab samples were compared with the bed shear stresses under ice cover. Fig. 49 shows the comparison.

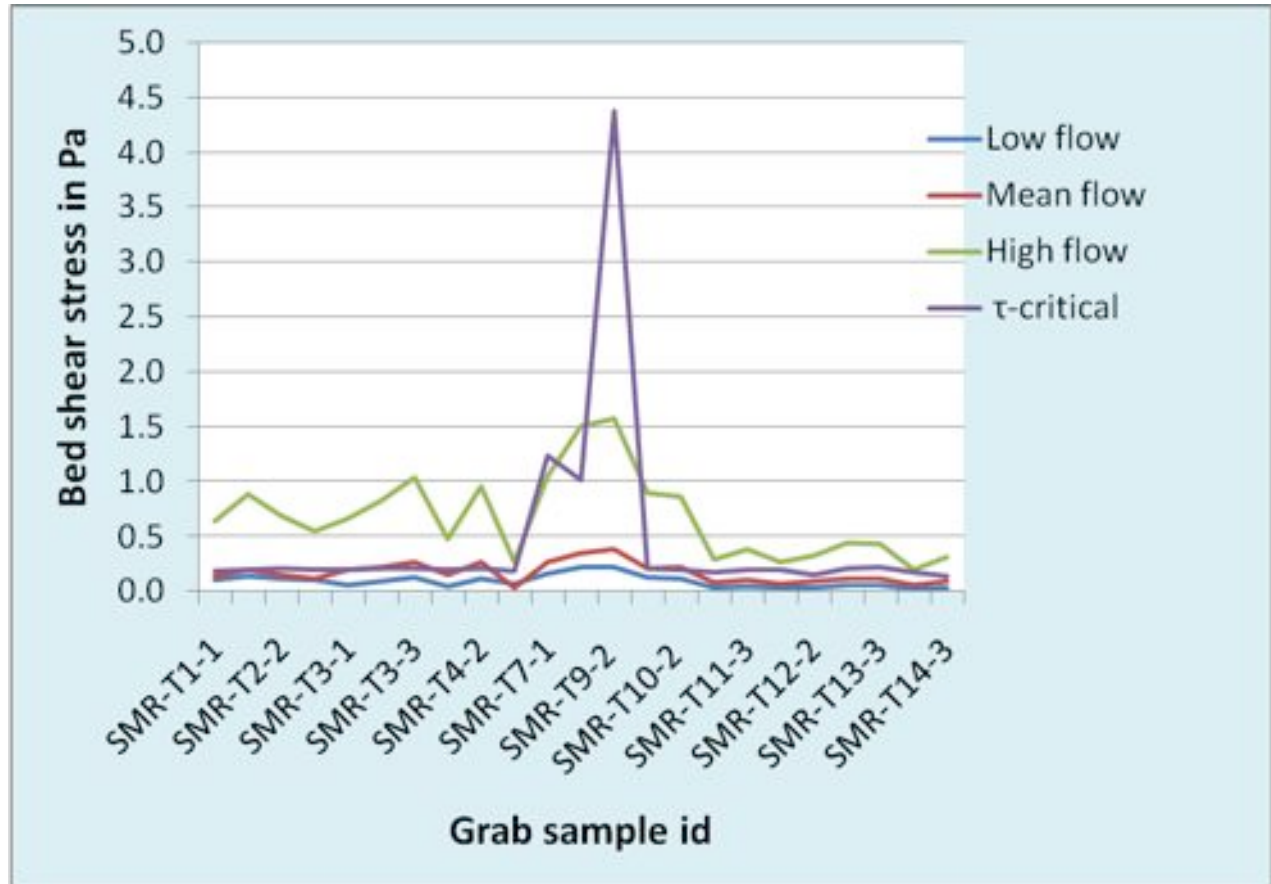


Fig. 49. Comparison of bed shear stress with critical shear stress for ice-covered flows.

From Fig. 49, we can see that the shear stresses for both low flow and average flow are below the critical shear stress for all non-cohesive grab samples. Only the shear stresses for high flows are above the critical shear stress. This means that the sediment is likely to be deposited during low and average flow conditions when the flow is ice covered. Only the high flow will be able to move the sediment when it is covered with ice.

The stability of the cohesive sediment under ice-covered flows is assessed in Table 5.

Table 5. Location of flume sites with ice-covered shear stresses and the critical shear stress.

Flume site id	Location of flume sites		Bed shear stress in Pa			τ -critical Pa
	Northing	Easting	Low flow	Mean flow	High flow	
10SSM_ISF32	5153419	705884	0.014	0.020	0.127	0.05
10SSM_ISF01	5153418	706079	0.014	0.012	0.081	0.05
10SSM_ISF_vortex	5152793	707714	0.001	0.001	0.004	0.05
10SSM_ISF09	5152659	708017	0.019	0.017	0.060	0.05
10SSM_ISF04	5152549	707788	0.032	0.047	0.148	0.05

From Table 5, we can see that the shear stresses of the ice covered flows at flume sites are far less than the critical shear stress for both low and average flows. Only the high flow will be able to move the cohesive sediment at four of the five sites tested. The sediment at the 10SSM_ISF_vortex site is stable even at high flows when it is ice-covered.

From the above results, we can see that the sediment in all areas of the St. Marys River is more stable under ice-covered flows than under the free surface flows. It should be pointed out here that the above calculations were carried out under the assumption that the river is covered with ice fully (i.e. full ice-cover). When the cover is partial, normally, the central part of the river will be open and the ice cover will be present on either side. This means that the flow at the open central part could see some increase due to the reduction of flow through the ice cover on either side. Since the central part of the river is covered with large stones, cobbles and pebbles, their stability will not be affected by this increase in flow. Therefore, we can still conclude that the stability of the sediment along the edges of the river and in re-circulation zones will be maintained even under partial ice covers.

Since the bed shear stresses under ice-covered flows are lower than that for the open water flows, it is likely that the sediment that is in motion in open water flow could start to deposit when the ice cover begins to form in winter. It can then be remobilized when the ice breaks up in the spring. Therefore, one could see an annual cycle of erosion and deposition of a certain fraction of the sediment in the St. Marys River in addition to the long term cycle of erosion and deposition due to long term flow variation.

10.1. Impacts of ice scour:

The potential impact of ice scour on the stability of sediment in the St. Marys River is linked to the possibility of occurrence of ice-jams in the river reach under consideration. When analyzing the ice scour potential in the St. Clair River near Sarnia, Beltaos (2010) made some general observations that are equally applicable to the present study. As a background for the ice scour process, Beltaos (2010) identified two types of ice scour effects; direct and indirect. The direct effect relates to a limited scour

that can occur near the head (upstream end) of the jam and a pronounced scour that can occur near the toe (downstream end) of the jam. The indirect effect is related to the potential scour due to abrupt release of ice jam during break up. He also noted that the scouring potential is more pronounced within the main channel than in shallow areas near the banks. As the central part of the St. Marys River is well armoured with large stones and cobbles, impacts of ice scour either direct or indirect are likely to be minimal in this part of the river. Since the bed shear stresses near the edges of the river as predicted by the model are small, the impact of ice scour due to ice jams on the cohesive sediment deposits near the edges of the river will also be small.

Beltaos (2010) also identified other potential ice effects such as ice gouging due to moving ice plates, water freezing into the bed near the banks and ice carrying away some sediment when it detaches from the bed at the time of breakup. To evaluate sediment erosion risks associated with these processes, Beltaos (2010) recommends in-situ field observations in the St. Marys River over a period of 2-3 winters.

11.0 Transport characteristics of eroded and/or introduced sediment in the river

Transport of fine sediment entering the river from upstream and/or mobilized within the river system can be modelled using the RMA4 model. An example of the RMA4 predictions is given here for the case of fine sediment entering from upstream. A hypothetical, constant source of 250 mg/L sediment is assumed for this example. RMA4 model uses the flow characteristics predicted by RMA2 for calculating the advective and dispersive fluxes of sediment as the sediment is transported downstream. The predictions shown below are for the case of the average flow. The predictions for low and high flows are shown in Appendix-C. The concentration profiles of the sediment for different elapsed times are shown in Figs. 50 to 54.

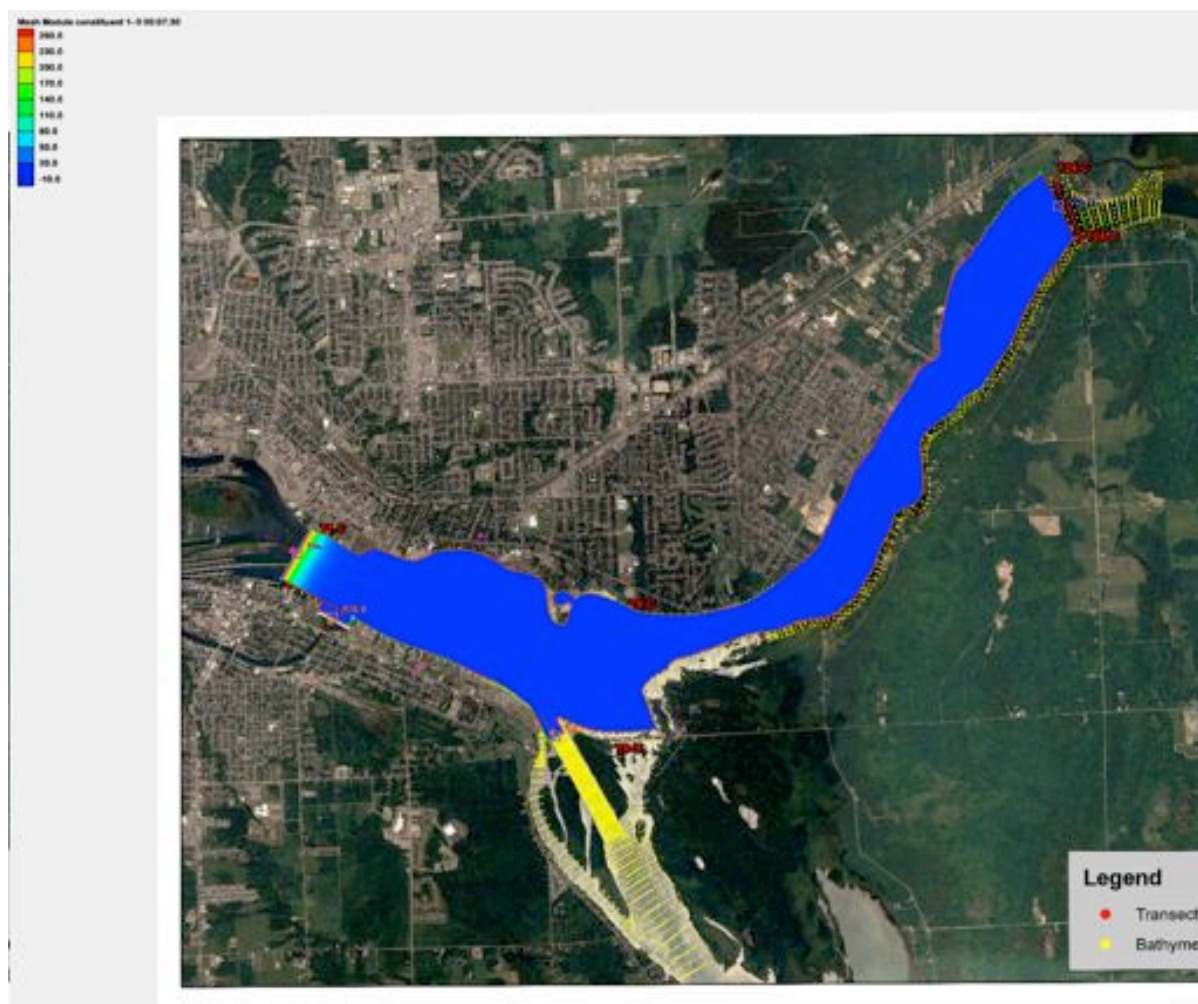


Fig. 50. Simulation of sediment transport in St. Marys River: Elapsed time = 0.125 hrs.

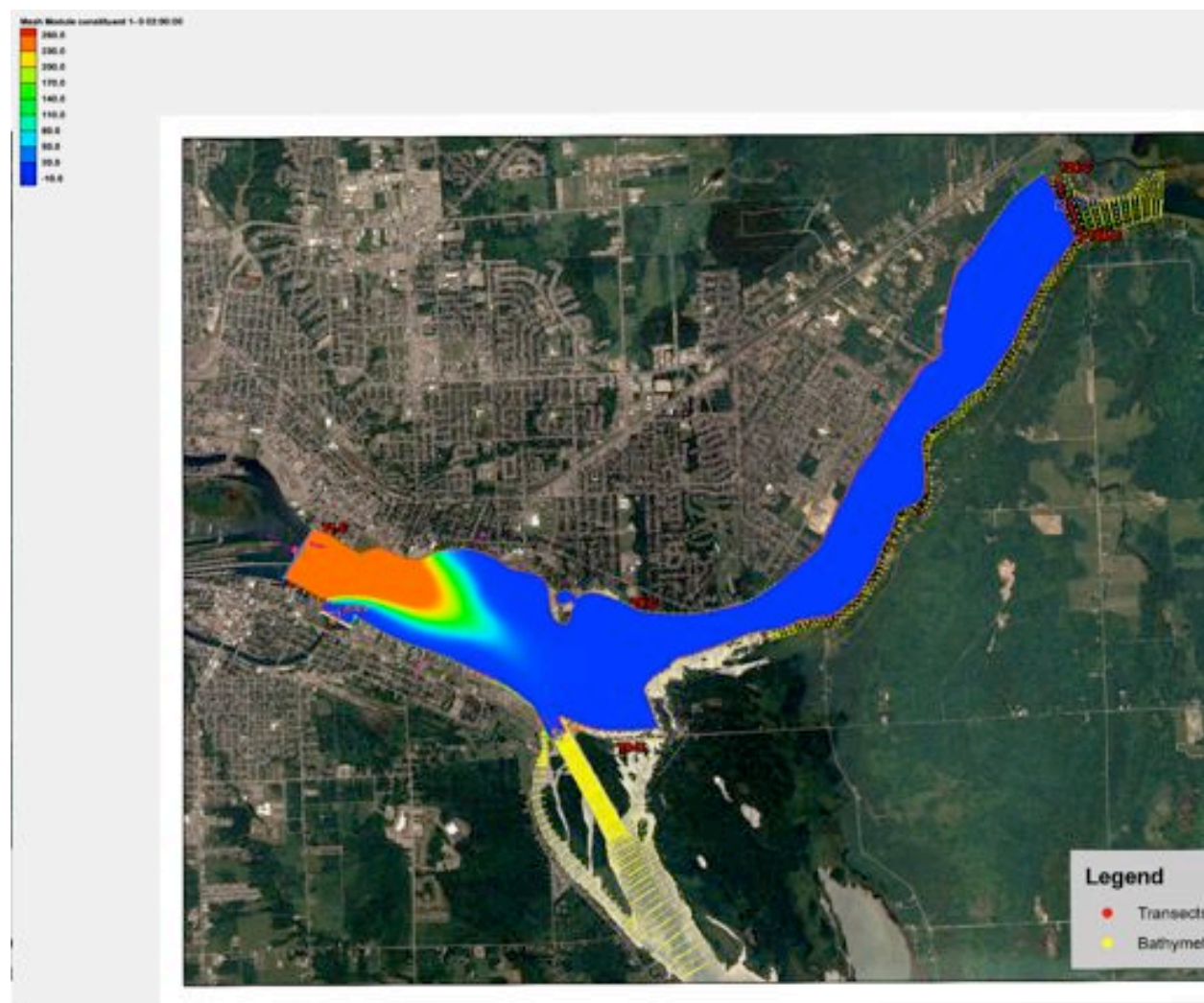


Fig. 51. Simulation of sediment transport in St. Marys River: Elapsed time = 2.0 hrs.

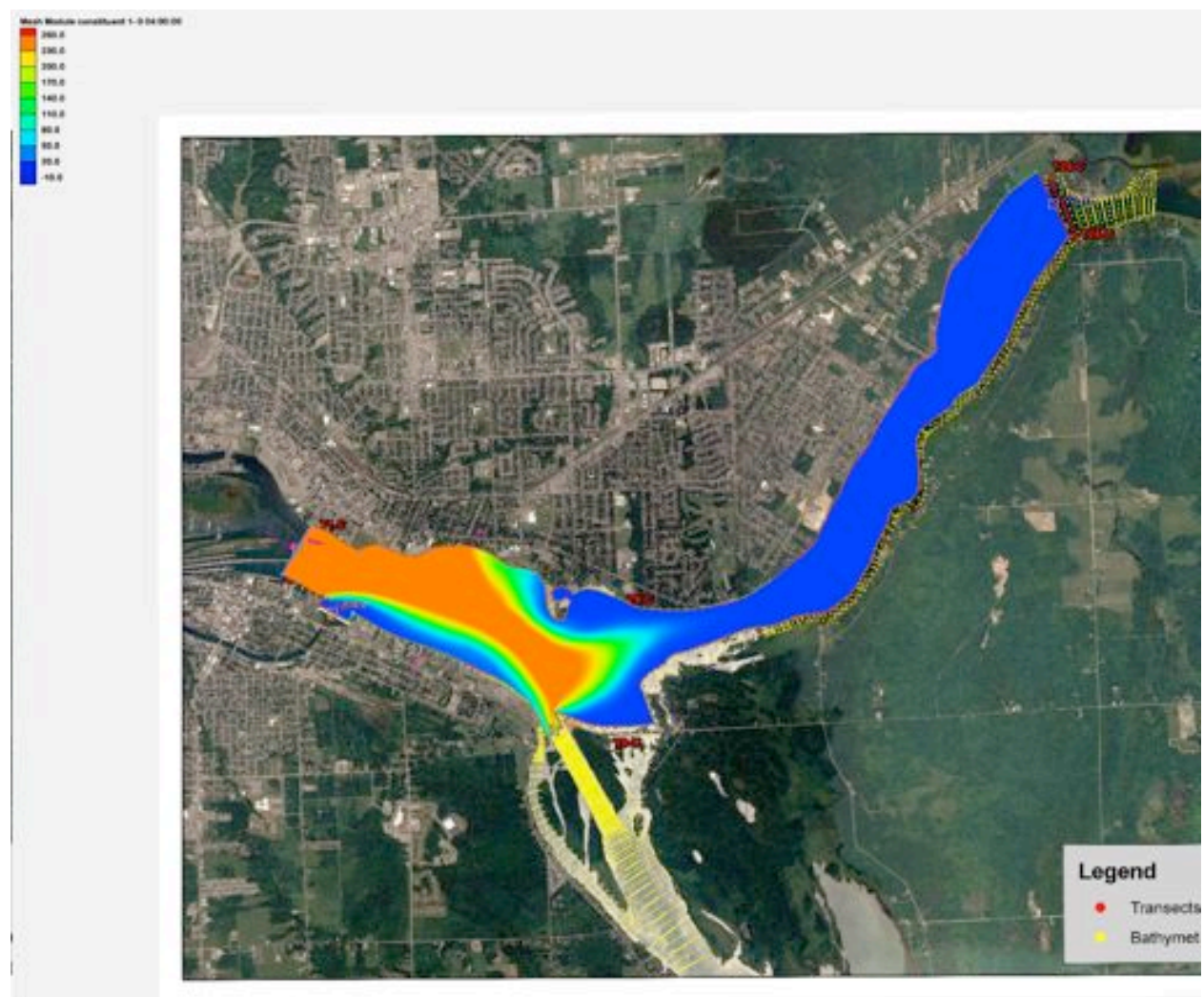


Fig. 52. Simulation of sediment transport in St. Marys River: Elapsed time = 4.0 hrs.

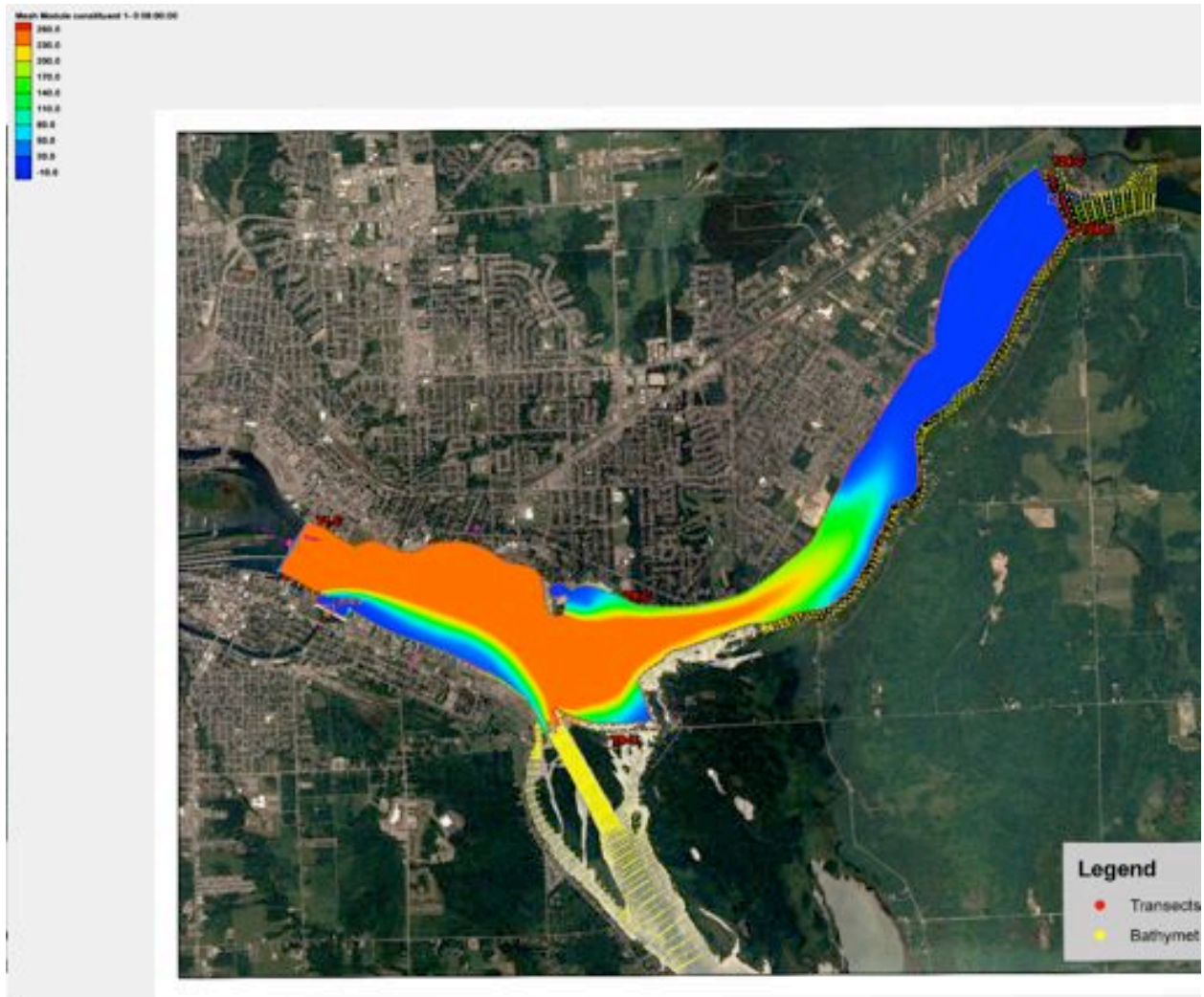


Fig. 53. Simulation of sediment transport in St. Marys River: Elapsed time = 8.0 hrs.

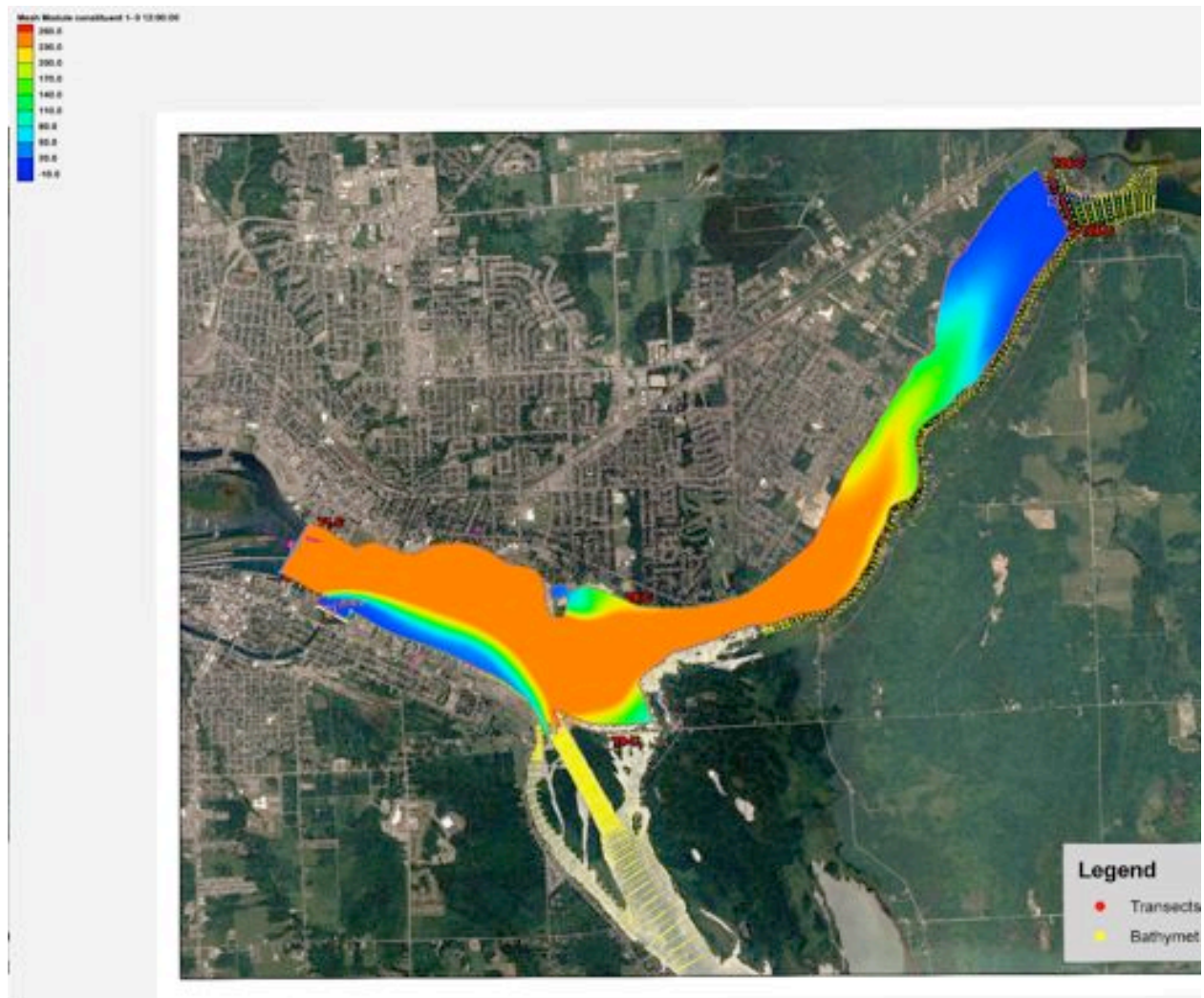


Fig. 54. Simulation of sediment transport in St. Marys River: Elapsed time = 12.0 hrs.

From the above figures, we can see the development of the sediment plume as a function of time. We can also see from these figures that the discharge from the Edison Sault Hydro Electric Power Plant deflects the sediment plume upwards and limits the amount of sediment entering the navigational channel. When the power plant discharge is switched off, then the sediment plume goes through the navigational channel un-hindered and the bulk of the sediment is transported through the navigational channel.

The simulations presented in appendix-D show clearly the dependency of the sediment plume on the flow characteristics. For low flow, the plume is much smaller in comparison to the plume for the high flow for a particular elapsed time. This example of sediment simulation demonstrates the capability of the model for predicting the sediment transport in the St. Marys River.

12.0 Summary and conclusions

A flow and sediment transport modelling approach is proposed for the St. Marys River to assess the physical stability of the surface and subsurface contaminated sediment deposit in the river. This modelling study aids in determining whether active management action is required for contaminated sediment deposits in the river.

Based on measured flow and sediment bed characteristics, a two dimensional flow modeling system called TABS-MD with SMS user interface was selected for the modelling approach. TABS-MD consists of a two dimensional hydrodynamic flow model (RMA2) and a fine sediment transport model (RMA4). The predictions of flow and sediment transport by the proposed TABS-MD modelling system with SMS user interface and the field measurement of sediment characteristics using video imaging, grab sampling and in-situ erosion flume provided us with the ability to assess the stability of the sediment in the St. Mary's River and to evaluate the options for sediment remediation.

The predicted bed shear stresses for different flow-rates with their associated water levels are compared with the critical shear stress for erosion of sediment to assess its stability under different flow regimes. Effects of ice cover on flow and sediment stability are also assessed. Potential impacts of ice scour process are discussed. The results of the present study indicated that the deeper layers (below ~5cm from the top surface) of contaminated sediment deposits along the edges of the river are stable.

The results from this study will be useful for developing management strategies for the contaminated sediment deposits in the modelled river reach.

Acknowledgements

A number of individual from various government agencies had provided assistance to this study. The author wishes to thank them all and also the St. Marys River Sediment Technical Team for providing valuable comments and the direction for this study. In particular, special thanks go to Mr. Eric Tauriainen, Mr. Tom Dankert and Mr. Calvin Creech of the Great Lakes Hydraulics and Hydrology Office of the United States Army Corps of Engineers for providing the Bathymetry and ADCP data for the study. Mr. Aaron Thompson of Boundary Waters Issues of Environment Canada provided assistance with the RMA2 model. Mr. Pat McCurry of Water Survey of Canada assisted with the acquisition of the ADCP data. Mr. Rob Caldwell of Great Lakes-St. Lawrence Regulation Office, Environment Canada in Cornwall, Ontario provided flow data for the model. Mr. Hans Biberhofer of Aquatic Ecosystem Management Research Division, National Water Research Institute in Burlington provided data on video imaging of the river bed, grab sample collection and analysis and in-situ erosion flume experiments. Mrs. Marilyn Dunnett of National Water Research Institute performed the analysis of the bathymetry data and generated the cross sectional data for the model study.

References

Beltaos, S. 2010. Personal communication.

Biberhofer, Hans. 2010. Personal communication.

DaSilva, A.M.A.F. and Bolisetti, T. 2000. A method for the formulation of Reynolds Number functions. *Canadian Journal of Civil Engineering*, 27(4): 829-833.

Dunnell, Barbara, P. , Letter, Joseph V., McNally, W.H., and others, Users Guide for RMA2 Version 4.5, 09 May, 2008, [<http://chl.wes.army.mil/software/tabs/docs.htm>]

Gatto, L.W. 1991. Ice conditions in the St. Marys River and selected harbours from 15 February to ice off. Unpublished contract report for the Detroit District, Corps of Engineers, Detroit, Michigan.

Gebhardt, K., D. Fielder, S. Greenwood, H. Robbins and T. Suttons (Editors) 2002. St. Marys River Fisheries Assessment Plan, Great Lakes Fisheries Commission Special Report, Ann Arbor, 46 pages.

Krishnappan, B.G. 1983. Suspended sediment profile for ice-covered flows. *Journal of Hydraulic Engineering*, ASCE, 109(3):385-399.

Krishnappan, B.G. 1984. Laboratory verification of a turbulent flow model. *Journal of Hydraulic Engineering*, ASCE, 110(4): 500-514.

Lau, Y.L. and Krishnappan, B.G. 1985. Sediment transport under ice cover. *Journal of Hydraulic Engineering*, ASCE, 111(6): 934-950.

Letter, J.V., Donnell, B.P. and Brown, G.L. 2008. Users Guide for RMA4 Version 4.5. [<http://chl.wes.army.mil/software/tabs/docs.htm>].

Norton, W.R., King, I.P. and Orlob, G.T. 1973. A finite element model for Lower Granite Reservoir, Walla Walla District, US Army Corps of Engineers, Walla Walla, WA.

Tauriainen, Eric. 2010. Personal communication.

Thompson, Aaron. 2010 Personal communication.

Yalin, M.S. and Karahan, E. 1979. Inception of sediment transport. *Journal of Hydraulics Division*, ASCE, 105(11): 1433-1443.